Narrow equilibrium window for complex coacervation of tau and RNA under cellular conditions

Yanxian Lin[1]*, James McCarty[2]*, Jennifer N. Rauch[3,4], Kris T. Delaney[5], Kenneth S. Kosik[3,4], Glenn H. Fredrickson[5,6], Joan-Emma Shea[2,7], Songi Han[2,6]†

* equal contributions

† corresponding author

1. Biomolecular Science and Engineering, University of California Santa Barbara, Santa Barbara, CA 93106, USA
2. Department of Chemistry and Biochemistry, University of California Santa Barbara, Santa Barbara, CA, 93106, USA
3. Molecular, Cellular and Developmental Biology, University of California Santa Barbara, Santa Barbara, CA 93106, USA
4. Neuroscience Research Institute, University of California Santa Barbara, Santa Barbara, CA 93106, USA
5. Materials Research Laboratory, University of California Santa Barbara, Santa Barbara, CA 93106, USA
6. Department of Chemical Engineering, University of California Santa Barbara, Santa Barbara, CA 93106, USA
7. Department of Physics, University of California Santa Barbara, Santa Barbara, CA 93106, USA

Abstract

The mechanism that leads to liquid-liquid phase separation (LLPS) of the tau protein, whose pathological aggregation is implicated in neurodegenerative disorders, is not well understood. Establishing a phase diagram that delineates the boundaries of phase co-existence is key to understanding whether LLPS is an equilibrium or intermediate state. We demonstrate that tau and RNA reversibly form complex coacervates. While the equilibrium phase diagram can be fit to an analytical theory, a more advanced model is investigated through field theoretic simulations (FTS) that provided direct insight into the thermodynamic driving forces of tau LLPS. Together, experiment and simulation reveal that tau-RNA LLPS is stable within a narrow equilibrium window near physiological conditions over experimentally tunable parameters including temperature, salt and tau concentrations, and is entropy-driven. Guided by our phase diagram, we show that tau can be driven towards LLPS under live cell coculturing conditions with rationally chosen experimental parameters.

Introduction

Protein liquid-liquid phase separation (LLPS) is a process in which proteins assemble and partition into a protein-dense phase and a protein-dilute phase. The proteins in the dense phase form droplets, and retain liquid-like mobility, as shown by NMR measurements (1,2). The process of LLPS *in vitro* has been observed for decades (3–8), but the field has recently been invigorated by the realization that LLPS also occurs *in vivo*, suggesting a possible physiological role for these assemblies(4,9,10). The overwhelming majority of proteins observed to undergo LLPS are intrinsically disordered proteins (IDPs) (11), and much of the research thus far has focused on ALS-related IDPs, including FUS (9,12–14), hnRNPA2B1 and hnRNPA1 (15), TDP-

43 (15,16), C9ORF72 (17–19) and Ddx4 (20). Recently, we and others discovered that another amyloid forming IDP, the microtubule binding protein tau, also undergoes LLPS (21–25). Interestingly, many of the LLPS forming IDPs have been observed to form amyloid fibrils in cell-free systems (13,15), leading to a number of hypotheses regarding the physiological role of LLPS in regulating aggregation. In particular, a compelling idea is that protein LLPS may be an intermediate regulatory state, which could redissolve into a soluble state or transition to irreversible aggregation/amyloid fibrils (13–15,21,22).

In a healthy neuron, tau is bound to microtubules. When tau falls off the microtubule under adverse conditions to the cell, tau is solubilized in the intracellular space as an IDP. Under certain conditions, tau forms intracellular fibrillary tangles, a process linked to neurodegenerative tauopathies that include Alzheimer's disease. In recent work, we showed that tau in neurons strongly (nanomolar dissociation constant) and selectively associates with smaller RNA species, most notably tRNA (22). We also found tau and RNA, under charge matching conditions, to undergo LLPS (22) in a process determined to be complex coacervation (CC) (26). We found that tau-RNA LLPS is reversible, and persisted for > 15 hours without subsequent fibrilization of tau, and hypothesized that LLPS is potentially a physiological and regulatory state of tau.

In this work, we characterize the phase diagram of tau/RNA LLPS using a combination of experiment and simulation, and thereby specify the conditions that drive the system towards a homogeneous phase or an LLPS state. We study a N-terminus truncated version of the longest isoform of human 4R tau *in vitro*, and first demonstrate that tau/RNA complexation is reversible, and that tau remains dynamic and without a persistent structure within the dense phase. The phase coexistence curve separating a supernatant phase from a condensate phase is determined

by the system's free energy, which in turn is state dependent, *i.e.* dependent on concentration, temperature, salt, and the nature of the interaction strength between the various solution constituents, including the solvent. We construct the phase diagram from cloud-point measurements of the onset of complex coacervation under varying conditions of temperature, salt, and polymer concentrations. These experiments establish the features and phase coexistence boundaries of the phase diagram, which we then model using theory and simulation to rationalize and understand the physical mechanisms that drive and stabilize LLPS.

A number of theoretical models can be used to model LLPS, each with their own advantages and disadvantages. Ideally, one would turn to simulations at atomic resolution in explicit solvent; however, such models are computationally prohibitive given the multiple orders of magnitude in time and length scales involved in LLPS. Turning to the polymer physics literature, theoretical treatments of simplified coarse-grained models are much more computationally tractable, and offer useful insight. Although approximate, analytical theories can be formulated, providing an extremely efficient platform for describing the thermodynamics of polyelectrolyte mixtures (27). These include the Flory-Huggins model (28), the Voorn-Overbeek model (6,29–34), the random-phase approximation (35–37), the Poisson-Boltzmann cell model (38,39), as well as other more sophisticated approaches(40–42), which have been applied to synthetic polymers with low sequence heterogeneity (29,43–46), and to proteins with single composition (2,20,47,48). While such models have been successful in describing simpler polyelectrolytes, it is less apparent that these models are suitable to describe the complex coacervation of the more complicated tau/RNA system. The simplest approach that one can use is the Flory-Huggins (FH) model, augmented by the Voorn and Overbeek (VO) correction to describe electrostatic correlations. This model is widely used to model LLPS; however, while

experimental data can be fit to the model (2,20), ultimately the FH-VO model has serious inadequacies. The original Flory-Huggins model is a mean-field theory, which means that fluctuations in polymer densities away from their average value in each phase are neglected. Augmenting the FH model with a VO treatment of electrostatics approximately accounts for charge correlations, but it entirely neglects chain-connectivity (49). Thus, the FH-VO model is unable to model the spatially varying charge distribution along the polymer backbone. Ideally, one would like to introduce chain connectivity, charge correlation, and uneven charge distribution into a more realistic polymer physics model; however, a full treatment of polymer density fluctuations is analytically intractable. One possible approach is to pursue a Gaussian approximation to field fluctuations, also known as the random phase approximation (RPA) (50–52). The RPA model can be viewed as a lowest-order correction to the mean field approximation, and was recently introduced to describe the charge pattern and sequence-dependent LLPS of IDPs (53,54). The advantage of the RPA model, over the mean-field FH-VO model, is that charge correlations are introduced in a formally consistent manner. Nonetheless, it has been recently demonstrated that the RPA model fails to quantitatively predict polymer concentrations in the dilute phase, given that higher-order fluctuations are important in this regime (55,56).

Of all the models described above, fitting experimental data with the FH or FH-VO theory is currently the preferred methodology in the LLPS community to describe and analyze phase diagrams. We demonstrate that this model can be fit to describe our experimental data, but the learning outcome from this modeling is limited. Thus, we take a different approach by computing the exact phase diagram of an off-lattice coarse-grained polyelectrolyte model using field theoretic simulations (FTS). FTS is a numerical approach that allows one to fully account

for fluctuations, and thus to compute equilibrium properties from a suitably chosen coarse-grained representation of the true system without the need for analytical approximation. The ability to perform field theoretic simulations enables us to include the important physics of polymer sequence-specificity that cannot be captured by FH-VO, including charge distribution and chain connectivity. Results from FTS are compared to those obtained from the FH-VO model.

The model substantiates the experimental phase diagram that the equilibrium window for the complex coacervation of tau and RNA under cellular conditions is narrow. Guided by the phase diagram, empirically obtained from *in vitro* experiments and validated by simulation, we finally show that LLPS of tau-RNA can be established and rationalized under cellular co-culturing conditions in the presence of live cells.

Results

Tau-RNA complex coacervate is reversible and a dynamic liquid phase.

Truncated versions of the longest isoform of human 4R tau, residues 255-441 (57) and residues 255-368 were used to study tau-RNA complex coacervation (CC). A C291S mutation was introduced to either tau variant, resulting in single-cysteine constructs. Thioflavin T assays and TEM imaging were performed showing these variants retain the capability to form fibrils with morphology similar to full length tau. Unless otherwise specified, we refer to these two single-cysteine tau constructs as tau187 and tau114 (tau114 is close to K18, 244-372 (58)), respectively, while tau refers collectively to any of these variants (see Materials and Methods for experimental details). Importantly, experiments were performed with freshly eluted tau within 30

minutes upon purification to minimize the effects of possible disulfide bond formation. This minimizes the influence of the cysteine mutations on the LLPS behavior of tau-RNA CC. The single-cysteine containing tau187 can be singly spin labeled at site 322, referred to as tau187-SL (see Materials and Methods). Full length tau, tau187 and tau114 are overall positively charged with an estimated +3, +11 and +11 charge per molecule at neutral pH, respectively, based on their primary sequences. The charged residues of tau are more concentrated in the four repeat domains (Fig. 1A). PolyU RNA (800~1000 kDa), which is a polyanion carrying 1 negative charge per uracil nucleotide, was used in this study and henceforth referred to as RNA (Fig. 1A). Under ambient conditions, both tau and RNA are soluble and stable in solution. By mixing tau and RNA under certain conditions, a turbid and milky suspension was obtained within seconds, where tau and RNA formed polymer-rich droplets (dense phase) separated from polymer-depleted supernatants (dilute phase) (Fig. 1B). These polymer-rich droplets are tau-RNA CCs. We began by determining the concentration of the dense and dilute phases. After mixing and centrifuging 60 μL tau187-RNA droplet suspension, we separated a polymer-rich phase of volume <1 μL with a clear boundary against the dilute supernatant phase. Applying UV-Vis spectroscopy (see Materials and Methods), we determined the concentration of tau and RNA inside the droplets as >76 mg/mL and >17 mg/mL with partitioning factors of >15 and >700 respectively. This is consistent with our previously findings that tau is virtually exclusively partitioned within the dense phase (22). High protein concentrations are typically correlated with higher propensity for irreversible protein aggregations. In order to verify that there was indeed no fibril formation, tau187-RNA CCs were prepared by mixing tau187-SL and RNA (see Materials and Methods) and monitored by continuous wave electron paramagnetic resonance spectroscopy (For details of cw-EPR experiments see Materials and Methods). The cw-EPR

spectra shows no broadening (Fig. 1C), and the cw-EPR spectra analysis reveals an unchanged rotational correlation time for the spin label of tau187-SL, τ, of 437 ± 37 ps as a function of time after > 96 hours of incubation at room temperature (Fig. 1D, turquoise) (see Materials and Methods). For comparison, cw-EPR spectra and τ were recorded of tau187-SL alone in buffer, and of tau187-SL in the presence of heparin under fibril forming conditions. Tau187-SL alone in buffer showed cw-EPR spectra overlapping with those of tau187-RNA CC, and rotational correlation time τ, 425 ± 16 ps, nearly identical to the τ of tau187-SL CCs (Fig. 1D, red). In contrast, tau187-SL with heparin shows a significantly broadened cw-EPR spectrum and an increasing τ to 2.3 ± 0.7 ns (Fig. 1C, D, green). Note that a hundreds of ps range of τ corresponds to rapid tumbling of the spin label, whose rotational degree of freedom is minimally hindered by molecular associations, while a several ns range of τ corresponds to slow tumbling and molecular hindering by association or confinement. The Thioflavin T (ThT) fluorescence curves of the same sample system as a function of time confirms the absence of amyloid aggregate formation in tau187-RNA CCs (Fig. S1). These results together suggest that tau187-RNA CCs are in an equilibrium state, in which tau retains its solution-like dynamics.

Next, we investigated the reversibility of tau187-RNA complex coacervation. Tau187-RNA CCs were prepared again and incubated by cyclically ramping the temperatures (1 °C/min) upwards and downwards, while the absorbance at = 500 nm was monitored, referred to as turbidity hereafter. Ramping rates of 0.5 °C/min and 1 °C/min were tested, but the results shown to be indistinguishable. Microscopy images were concurrently acquired at low and high turbidity, confirming the appearance and abundance of CC droplets correlating with turbidity increase, and *vice versa* (Fig. 1E). The turbidity-temperature curves show that at high temperature, samples became turbid with Abs_{500} ~ 1.5 and abundance of CCs, while at low temperature, samples

became transparent with $Abs_{500} \sim 0$ and absence of CCs. This demonstrates tau187-RNA CC formation is favored at higher temperature, following clearly a lower critical solution temperature behavior (LCST) (Fig. 1E) (59). By cycling the temperature, we robustly and reversibly changed the tau187-RNA mixture between a turbid state to a completely transparent state (Fig. 1E). The transition temperatures at which the turbidity emerged during heating and vanished during cooling stay invariant with repeated heating-cooling cycles. The method of extracting a cloud point for the LCST transition temperature from such data will be described in detail in the next section. Importantly, the history of temperature change does not affect the resulting state. Hence the formation and dissolution of tau187-RNA CCs are reversible and consistent with a path-independent equilibrium process. We point out that the maximum turbidity value successively decreases with each heating cycle (Fig. 1E), even though the transition temperatures remain invariant. This can be attributed to slow degradation of RNA with time, (as demonstrated in Fig. S2) by verifying an altered turbidity change in the presence of RNase or RNase inhibitor.

It is understood that upon gradual heating of the solution phase, the mechanism of LLPS proceeds via a nucleation process (60), and hence there is a kinetic barrier evidenced by the observed hysteresis in Fig. 1E. Nonetheless, we conclude that the final tau-RNA CC state reached upon heating is a true thermodynamic state, and thus can be modeled by an equilibrium theory of phase separation.

Tau-RNA complex coacervate phase diagram

To understand the principles and governing interactions driving tau-RNA CC formation, we constructed a phase diagram for tau187-RNA CC by measuring the transition temperature –

to be described in greater detail below – as a function of protein concentration and salt concentration. We first recorded tau187-RNA turbidity at various [tau], [RNA] and [NaCl] values, ranging from 2-240 μM, 6-720 μg/mL and 30-120 mM, respectively. Titrating RNA to tau187, the turbidity was found to be peaked when [RNA]:[tau] reached charge matching condition at which the charge ratio between net positive and negative charges was 1:1 (which for tau187 and RNA used in this study corresponded to [tau187]:[RNA] = 1 μM : 3 μg/mL), validating once more that LLPS is driven by complex coacervation (CC) (Fig. S3). Henceforth, all phase diagram data are acquired at a charge matching condition between RNA and tau. Titrating NaCl to tau187-RNA, CC formation showed a steady decrease of turbidity (Fig. S3). Combined, these demonstrate that tau187-RNA CC favors the condition of charge balance and low ionic strength, which is consistent with known properties of CC and previous findings (22).

We next investigated the phase separation temperatures under various sample compositions. Tau187-RNA CCs were prepared with a fixed [tau]:[RNA] ratio corresponding to the condition of net charge balance. Therefore, the composition of tau187-RNA CC can be determined by [tau] and [NaCl]. Samples were heated at 1 °C/min between T = 15-25 °C, while the turbidity was monitored. The turbidity-temperature data of the heating curves were then fit to a sigmoidal function, so that the cloud point temperature, T_{cp}, could be extracted as shown in Fig. 2A (T_{cp} was determined from heating curves out of practical utility; T_{cp} from cooling curves is possibly closer to thermodynamic transitions). The experimental cloud-point temperature T_{cp} for CC formation as a function of [tau] and [NaCl] are shown (as points) in Fig. 2B and Fig. 2C. The experimental data points show that increasing [tau] lowers T_{cp}, favoring CC formation, while increasing [NaCl] raises T_{cp}, disfavoring CC formation. Such trends were observed at two

[NaCl] and two [tau] values, respectively (Fig. 2B, 2C). Experimentally, T_{cp} was determined for a range of [tau] and [NaCl] conditions (see Fig. S4).

The features of the Tau-RNA CC phase diagram were also investigated by comparing tau187 and tau114. Tau187-RNA CC and tau114-RNA CC were prepared with 20 μM tau187 and 28 μM tau114, so that the total concentration of polymer, i.e. tau and RNA, reaches 0.5 mg/mL. Turbidity was recorded at varying [NaCl]. Similar to the observation with tau187-RNA CC, tau114-RNA CC showed decreasing turbidity at increasing [NaCl] (Fig. S5). The [NaCl] values where turbidity reaches 0 were estimated as 131 mM and 150 mM for tau187 and tau114, respectively, implying CC formation is more favorable with tau114 that hence can sustain higher [NaCl]. Based on this, 20 μM of tau187, 131 mM of NaCl and room temperature, 20 °C, were used as the phase separation conditions ([tau], [NaCl] and T_{cp}) for tau187, and 28 μM, 150 mM and 20 °C for tau114. These two experimental conditions were used in the next section for comparing the two constructs of tau.

Flory-Huggins-Voorn-Overbeek Fit to Experimental Phase Diagram

We next used the FH-VO model to fit the experimental data for the tau187-RNA CC system, as is commonly done in LLPS studies. Despite its theoretical deficiencies the FH-VO model is commonly used for its simplicity and ease of implementation. Our system consists of five species: tau187, RNA, monovalent cation (Na^+), anion (Cl^-) and water. For simplicity, we explicitly consider only the effect of excess salt, and do not include polymer counterions. The FH-VO model maps these five species onto a three-dimensional lattice (Fig. 2D). Each polymer is treated as a uniform chain with degree of polymerization N and average charge per monomer σ. N was taken as the average chain length of the species (1 for monovalent ions). The charge

density σ of RNA, monovalent ions and water were set to 1, 1 and 0 respectively. The values for σ of tau187 or tau114 were calculated from the net charge at neutral pH divided by the chain length. The composition of the species is expressed in terms of the volume fraction ϕ of the occupied lattice sites, which are proportional to the molar concentrations (see Materials and Methods for details). As in experiments, tau187-RNA CCs were prepared at fixed [tau]:[RNA] and $[Na^+]$:$[Cl^-]$ ratios. Under these two constraints, the volume fraction of all five species in tau187-RNA CC listed above can be determined with two variables, [tau] and [NaCl], which are experimentally measurable.

Given N, σ, [tau], [NaCl] and T_{cp}, the task is to find ϕ_{tau}^{I} and ϕ_{tau}^{II}, the volume fractions of tau in the dilute and dense, coacervate, phase at equilibrium, i.e. the binodal coexistence points. The model and procedure is described in detail in the Materials and Methods. For each experimental observation of T_{cp} determined for a given [tau] and [NaCl] (Fig. S4), the FH-VO expression has one unknown parameter, the Flory-Huggins χ term. The Flory-Huggins χ parameter is introduced as an energetic cost to having an adjacent lattice site to a polymer segment occupied by a solvent molecule (61). Here we take χ to be an adjustable parameter, such that given a suitable expression for χ, the complete binodal curve can be modeled with the FH-VO theory. Consequently, we first solved for χ at each given experimental condition, so that the theoretical binodal curve intersects the experimental data point. Fig. 2E shows two representative examples of a theoretical binodal curve (solid line) intersecting a single experimental data point at the given [NaCl] and [tau]. This procedure gives an empirical χ parameter for each experimental data point, as collated in Fig. 2F as a function of $1/ T_{cp}$. We then performed to this set of experimental data a least-squares fit of the empirical χ parameter to the form A + B/T (Fig. 2F), yielding an expression of the temperature dependence of χ of

$$\chi\,(T) = 1.8 - \frac{390}{T},\ R^2 = 0.67. \qquad \text{(Equation 1)}$$

A temperature dependence of χ in the form of Equation 1 (consistent with the observed LCST), can originate from hydrophobic interactions between non-polar groups, whose interaction strength tends to increase with temperature (62,63). This explanation has also been used to describe cold denaturation of proteins (64).

Finally, from this expression for χ(T), we computed the binodal curves that establishes the phase coexistence as a function of T_{cp}, [tau] and [NaCl], shown as solid lines, only for the dilute phase coexistence for T_{cp} vs [tau] (Fig. 2B) and T_{cp} vs [NaCl] (Fig. 2C). For the full phase diagram showing both dilute and dense binodal curves see Fig. S6. The experimental data (shown as points) and computed binodal curves both exhibited a decreasing T_{cp} with increasing [tau] and an increasing T_{cp} with increasing [NaCl]. This simply establishes that tau-RNA CC favors higher tau concentrations in the 1-240 μM range and lower ionic strength in the 30-120 mM range tested here. Binodal curves for tau114-RNA CC were also computed, and are compared with tau187-RNA CC, along with experimental data (Fig. S5). Comparison of the two constructs shows that tau114-RNA CC has a lower T_{cp} than tau187-RNA CC, suggesting it is more favorable to phase separation. This qualitatively agrees with experimental observations. Note that the experimental conditions are for [tau] and [RNA] set at charge matching conditions for maximal CC, and thus [tau] and [RNA] are locked relative to each other. When [RNA] falls either well below or well above charge matching condition relative to [tau], it is expected that the LLPS envelope will collapse.

Field theoretic simulations of a coarse-grained model of tau-RNA complex coacervation

Although the FH-VO model can be brought into agreement with experiment through a judicious choice of χ, it is fundamentally unsound from a theoretical perspective, noticeably because it neglects connectivity between charges on the same chain. This is a severe limitation because it is expected that subtle difference in primary amino acid sequences may have a profound effect on the phase diagram. A particularly appealing alternative to gain insights into the thermodynamics of LLPS is to perform field theoretic simulations (FTS) on a physically motivated polyelectrolyte model (Fig. 3), in which each amino acid is represented by a single monomeric unit of length b in a coarse-grained bead-spring polymer model. The charge of each segment is unambiguously assigned from the particular amino acid charge at pH 7.0. In addition to harmonic bonds between nearest neighbors, which enforces chain connectivity, all segment pairs interact via two types of non-bonded potentials: a short-ranged excluded volume repulsion and a long-range electrostatic interaction between charged monomers (see Fig. 3). We take the polymers to be in a slightly good solvent, meaning that favorable interactions between monomers and solvent cause chain swelling. In such cases, the excluded volume interaction is modeled as a repulsive Gaussian function between all monomer pairs with a strength that increases with solvent quality (65). Conversely, as solvent quality decreases, the excluded volume repulsion decreases, approaching zero at the so-called theta condition. In the present case we limit ourselves to the case where the excluded volume is positive and small, i.e. a good solvent near the theta condition. Simulations are performed using a single excluded volume strength, v, identical for all monomers, which is an input parameter in the model and can be adjusted to parameterize the favorable monomer-solvent interactions. Additionally, the long-range electrostatic interactions are described by a Coulomb potential in a screened, uniform, dielectric background. The length scale of the

electrostatic interactions is parameterized by the Bjerrum length l_B, which is the distance at which the electrostatic interactions become comparable to the thermal energy k_BT and is defined as

$$l_B = \frac{e^2}{4\pi\epsilon_0\epsilon_r k_B T} \quad \text{(Equation 2)}$$

where e is the unit of electronic charge, ϵ_r the dielectric constant ($\epsilon_r = 80$ for water), and ϵ_0 the vacuum permittivity.

The main features of the model used for FTS here are the inclusion of chain connectivity, charge sequence-dependence for the electrostatic interactions based on the primary amino acid sequence of tau, solvation effects which are parameterized by the single excluded volume parameter, v, and an electrostatic strength parameterized by the Bjerrum length, l_B. FTS is performed in implicit solvent with a uniform dielectric background. We assume that the polymer chains are in a fully dissociated state, and we do not explicitly represent counter ions. The effect of excess salt is included in our model by introducing point charges explicitly, which engage in Coulomb interactions with all other charged species and repel other ions and polymer segments at short distances by the same Gaussian excluded volume repulsion. By introducing explicit small ions in this manner, we are neglecting strong correlations such as counter ion condensation; however, we are allowing for weak correlations of the Debye-Hückel type. The explicit addition of salt will serve to screen the electrostatic interactions and inhibit the driving force for CC, in agreement with the experiments.

Details of the FTS protocol are described in the Materials and Methods. By performing FTS at various state points and computing equilibrium properties, we first set out to fully explore the parameter space relevant for LLPS in this model. This involves running simulations at different conditions analogous to experiments. For each simulation the thermodynamic state of

the system is determined by specifying a particular value for the dimensionless excluded volume parameter v/b^3, the dimensionless Bjerrum length l_B/b, and the dimensionless monomer number density ρb^3. Fig. 4 shows the final polymer density configuration for two representative simulations at a monomer density of $\rho b^3 = 0.22$ at different thermodynamic conditions (see caption for Fig. 4 for details). Although the bulk density is fixed and identical for the two cases, the local polymer density is free to fluctuate. The left simulation box (Fig. 4) shows a case where a single phase is favored, indicated by a nearly homogenous polymer density throughout the simulation box (white/blue). This is contrasted by the right simulation box (Fig. 4) depicting the case where the system phase separates into a dilute polymer-deplete region (white) and a dense polymer-rich droplet region (red)—the coacervate phase with the color signifying the polymer density. Fig. 4 shows that given suitable parameterization, FTS can be used to study complex coacervation of a coarse-grained tau-RNA model. Given this observation, we next map out the full phase diagram in the parameter space of the model while fixing the physical parameters of charge sequence, chain length, and chain volume fractions that are consistent with the experimental conditions.

Field theoretic simulations predict phase equilibria around physiological conditions

The parameters to be explored in connection with phase behavior are the strength of the interactions in the polyelectrolyte model: the excluded volume strength v and the Bjerrum length l_B. A direct comparison between FTS and the experimental phase diagram will be deferred until the following section. The phase coexistence points (binodal conditions) for a given value of the excluded volume v and Bjerrum length l_B can be obtained by running many simulations over a range of concentrations, and finding the concentration values at which the chemical potential and

the osmotic pressure are equal in both phases (see Fig. S7). The procedure is described in the SI, and is repeated for many different v and l_B combinations. The resulting phase diagram will be a three-dimensional surface which is a function of ρ, v, and l_B. In Fig. 5A, we show a slice of this surface along the $l_B - \rho$ plane with a fixed value of $v = 0.0068\, b^3$, and in Fig. 5B we show a slice along the $v - \rho$ plane with a fixed $l_B = 1.79\, b$ (at T = 293 K, Eq. 3). It should be noted that Fig. 5 presents the first complete phase diagrams presented in the literature of a theoretical model describing a biological complex coacervate system. From Fig. 5, one can see that l_B and v have counteracting effects, namely increasing v that is caused by increased solvent quality destabilizes the coacervate phase and favors the single phase, whereas increasing l_B that is caused by reduced electrostatic screening favors coacervation, and destabilizes the single phase. The physical interpretation of the trends in Fig. 5 is that the actual binodal for the experimental system will depend on two competing features: the solvent quality proportional to v, which inhibits coacervation, and the electrostatic strength of the media proportional to l_B which promotes coacervation.

The FTS- derived phase diagram shown in Fig. 5 provides a guide how to experimentally tune the window for complex coacervation by changing the relative contribution of the solvent quality or the dielectric strength. Experimentally, the solvent quality can be decreased by adding crowding agents or by changing the hydrophilic/hydrophobic amino acid composition, while the electrostatic strength can be controlled by the salt concentration. Increasing salt concentration tends to decrease the bare electrostatic strength by screening the charges, and this is predicted to stabilize the single phase solution mixture against coacervation, in agreement with experimental observation. We explore these ideas further below in the context of tau coacervation *in vivo*.

Despite the simplicity of the coarse-grained description, the model predicts that these two competing parameters, excluded volume vs. electrostatic interactions, are nearly balanced around physiological salt concentration, temperature, and protein concentration. Assuming that the relative dielectric constant for water is $\epsilon_r = 80$, and that the segment size b is approximately equivalent to the distance between C_α carbons, i.e. b ~4 Å, it follows that $l_B = 1.75b$ at 300 K. ($l_B = 0.7\ nm$ at 300 K). In the $l_B - \rho$ plane (shown in Fig. 5A), at the cross section of $l_B = 1.75$, three points for ρb^3 are indicated that correspond to 1, 5, and 10 μM for tau concentrations at 300 K. Here we have implicitly assumed that at physiological temperature and in a crowded cellular environment tau is near the theta condition, and thus *v* is small. This analysis suggests that small modulation in the experimental conditions, such as changes in the temperature or salt concentration, local pH or crowding effects (via the excluded volume parameter v) can readily and reversibly induce complex coacervation *in vivo* under physiological conditions.

Comparison between simulation and experiment

In the preceding section we presented the phase diagram from FTS explicitly in terms of the model parameters of the excluded volume *v* and Bjerrum length l_B. We now seek to compare our simulation results directly with the experimental phase diagram. This requires knowing precisely how the model parameters depend on temperature. We again take the monomer size *b* to be approximately the distance between the C_α carbons b ~4 Å, and assume a dielectric constant of $\epsilon_w = 80$ for pure water. Although ϵ_r will depend on temperature, for simplicity we treat this parameter as a constant such that the Bjerrum length $l_B \sim 1/T$. Thus, l_B can be estimated at the

experimental cloud point temperature directly from Equation 2 (Fig. 6A), which leaves only one unknown parameter v.

The excluded volume parameter v can be related to the residue-residue non-Coulombic interaction potential as

$$v = \int_0^\infty [1 - e^{-\frac{U(r)}{k_B T}}] d^3 \qquad \text{(Equation 3)}$$

and is typically taken to be proportional to $(1 - \theta/T)$ where θ is the theta temperature, the temperature at which the chain follows ideal chain statistics (65–67). For LCST behavior it is customary to introduce the form $v = -v_0(1 - \theta/T)$ where v_0 controls the magnitude of the excluded volume interactions (68). This form of the excluded volume implies that at temperatures lower than the theta temperature, the excluded volume is repulsive ($v > 0$, meaning a good solvent) and for temperatures above the theta point, the excluded volume becomes attractive ($v < 0$, poor solvent conditions). By adjusting the excluded volume in FTS to fit a subset of the experimental data, (shown in Fig. 6B), we then perform a linear fit to obtain a value of $v_0 = 0.25b^3$ and $\theta = 309$ K. Note that in the range of temperatures considered, the excluded volume remains positive. However, for temperatures higher than θ, when the excluded volume becomes negative, the polymer chain will collapse, consistent with the observation in the literature (69), which showed that tau undergoes a thermal compaction at high temperatures due to entropic factors (66). In such high temperature regimes a more sophisticated treatment is needed; however, all our experimental conditions remain below this threshold. Having mapped the two model parameters v and l_B to the experimental temperature, we can compare directly the FTS with the experimental results (Fig. 6C). The calculated FTS data points under the condition of low salt concentration are shown as filled green squares in Fig. 6C.

Next, explicit salt ions were introduced as point charges to simulate an excess salt concentration of 120 mM. We make the assumption that the salt is equally partitioned in both phases, and thus the concentration of salt is a constant, allowing us to sweep the polymer concentration at fixed salt concentration to find the phase coexistence points. A more detailed FTS study of salt partitioning performed using a Gibbs ensemble method found that under conditions of nearly charge-balanced polymers, as is the case in the system of this study, the salts are nearly equipartitioned and counterion condensation is not a dominant factor (70). Simulations performed in this manner with explicit salt are shown as open green squares in Fig. 6C. The FTS data clearly demonstrate that the effect of added salt is to stabilize the single solution phase, and to raise the binodal closer to physiological temperature 37 °C, in agreement with experiments (filled red and blue circles Fig. 6C). The complementary dense branch of the binodal curve is also predicted from FTS and is shown in Fig. S8.

Application to cell-complex coacervate co-culture

Looking at the experimental and calculated phase diagrams (Fig. 2B, 2C), it is seen that under physiological conditions (T_{cp} ~ 37 °C, [NaCl] ~ 100 mM) it is principally feasible for cells to tune the formation of tau-RNA CCs. This has important implications for studying the physiological roles of tau-RNA CCs, and thus we asked if tau-RNA CCs could indeed exist in a biologically relevant media in the presence of living cells. Both the FH-VO theory and FTS predict that the conditions of high protein concentration, low ionic strength, high temperature and high crowding reagents (leading to solution conditions with a lower effective excluded volume parameter to model the poorer solvent environment) would independently favor tau-RNA CC formation. Using these tuning parameters as a guide, we designed several experiments

to test the ability for tau-RNA CCs to form in a co-culture with H4 neuroglioma cells. We incubated H4 cells with tau187/tau114-RNA under CC conditions at varying temperatures, polymer concentrations and crowding reagent concentrations. At low polymer concentrations (10 μM tau, 30 μg/ml RNA) no LLPS was observed in the cellular media (Fig. 7, first column), where increasing the temperature to 37 °C did not apparently influence the solution phase (Fig. 7, first column, first and third row). However, when tau and RNA concentrations were increased (100 μM tau, 300 μg/ml RNA) LLPS could be observed (Fig. 7, second column). Further, LLPS could also be achieved by adding an additional crowding reagent (here PEG) to low concentration samples of tau and RNA (Fig. 7, third column). As predicted, LLPS of tau-RNA CC was modulated by (i) temperature, (ii) tau and RNA concentration and/or (iii) the presence of crowding reagent PEG (Fig. 7). Lowering the temperature to 18°C significantly reduced the number and size of fluorescent droplets, demonstrating that tau-RNA LLPS is indeed tunable by temperature, and demonstrate the biological consequence of the LCST behavior (Fig. 7, first and third row). These results were consistently found for both tau187 and tau114 systems. The successful application of FTS for tuning and predicting tau-RNA CCs in cellular media is a first step towards understanding the physiological condition under which tau-RNA LLPS, which follows the CC mechanism, can occur. The conditions described for LLPS here suggests that conditions exist *in vivo* under which LLPS by complex coacervation may be achieved.

Discussion

The ability of tau to undergo LLPS via a mechanism of complex coacervation has been recognized in a number of recent publications (21,25) (22). However, to date, the criteria and

physical parameters (specifically, polymer concentration, ionic strength, temperature and crowding reagents) that drive tau-RNA CC has not been rationalized. In this paper, we mapped out the experimental phase diagram for tau-RNA CC, and used theory and simulation to describe the parameter space for LLPS. In what follows, we discuss the relevance of our findings in the context of the physical mechanism of LLPS *in vivo.*

Although the FH-VO model cannot model spatially varying charges along the peptide backbone, we were able to fit the experimental data by treating the Flory-Huggins χ parameter as an empirical, temperature-dependent, adjustable parameter. This result highlights the fact that the FH-VO model is adaptable to experimental data. Still, the FH-VO model has limited predictability, and should be seen as a qualitative descriptor of phase separation. In contrast, FTS is an approximation-free analysis that can provide physical insight and predictive information for biopolymers, such as scaling relationships and polymer or protein sequence effects. As shown above, the tau-RNA phase diagram was successfully reproduced by FTS using model parameters that are reasonable estimates of the experimental physical conditions. With reasonable estimates for the parameters in our polymer model ($\epsilon_r = 80$, $b = 4$ Å), our simulations predict that the lower phase boundary falls in the vicinity of physiological conditions. This finding suggests that FTS can be a powerful theoretical modeling technique to describe and rationalize tau-RNA CC as a competition between short-ranged excluded volume interactions and long-ranged electrostatic interactions.

Consider that we can partition the driving forces of CC as

$$\Delta G^{CC} = \underbrace{\Delta H^{tau/RNA}}_{(-)} - \underbrace{T\Delta S^{comb}}_{(-)} + \underbrace{\Delta H^{ex} - T\Delta S^{noncomb}}_{excluded\ volume\ or\ \chi}$$

where the first two terms are the negative (favorable) enthalpic contribution from tau/RNA interactions and the ideal entropy of mixing term (which is negative because we are considering

CC formation). These first two terms are approximately accounted for in the original VO model, and by themselves predict UCST behavior (see SI). The last two terms introduce an non-ionic excess enthalpic contribution and a nonideal, noncombinatoric entropy that are introduced into the FH-VO model through the Flory-Huggins χ parameter, or within FTS through the temperature dependent excluded volume. Given the experimental observation of LCST phase behavior, these terms must be important and we now estimate their value from our model.

Modeling the LCST experimental tau-RNA CC phase diagram using the FH-VO model by invoking an entropic term in the Flory-Huggins χ parameter, or by FTS using a temperature dependent excluded volume, both provide an estimate of the entropic contribution that drives CC formation. The temperature-dependent excluded volume v used to describe LCST phase behavior within FTS can be formally related to the Flory-Huggins χ parameter to second order in the polymer volume fractions $v = b^3(1 - 2\chi)$ (71). Substituting our empirical excluded volume, we obtain from FTS an interaction parameter χ of the form $\chi = \epsilon_s + \epsilon_H/T$, with ϵ_s being a non-combinatoric entropic term and ϵ_H an enthalpic term. Introducing conventional units (see Materials and Methods for details) gives an unfavorable non-electrostatic enthalpy of phase separation of ΔH^{ex} = 0.23 kJ • mol^{-1} of monomer, and a favorable noncombinatoric entropy of phase separation of $T\Delta S^{noncomb}$ = 1.1 kJ • mol^{-1} of monomer at T = 300 K. For comparison, the empirical χ from fitting the experimental data with the FH-VO model gives ΔH^{ex} = 2.3 kJ • mol^{-1} of monomer and $T\Delta S^{noncomb}$ = 3.24 kJ • mol^{-1} of monomer.

Notably, ΔH^{ex} is small and positive. We hypothesize that the positive, i.e. nonionic, enthalpy value for forming a coacervate phase is due to the requirement of breaking favorable interactions between hydrophilic residues and water that stabilizes the solution phase of tau ($\Delta H^{ex} = -\Delta H^{tau/water}$). For comparison, the enthalpy of forming a hydrogen bond ΔH_{HB} at room

temperature is ~ −8 kJ • mol^{-1} (72) while the enthalpy of hydration for a polar amino acid ΔH_{hyd} is ~ −60 kJ • mol^{-1} (73,74). Given that $\Delta H^{tau/RNA}$ for tau–RNA association is negative and tau remains hydrated in the CC state (i.e. tau-water interface is not dehydrated), there has to be a source of penalty in the form of a positive ΔH^{ex} value; the unfavorable ΔH^{ex} associated with tau-RNA CC might come from the loss of hydrogen bonds in the hydration shell from overlapping and sharing of the tau hydration shells in the dense CC phase.

The $T\Delta S^{noncomb}$ value is also small, positive and of comparable magnitude as ΔH^{ex}, making temperature increase a facile modulator favoring tau-RNA CC. Given the positive value of ΔH^{ex} for tau-RNC CC, the entropy gain upon phase separation is contributing to the driving force of tau-RNA CC formation (besides the electrostatic correlation energy between the polycationic and polyanionic polymer segments that is the major driving force). Looking to potential origins for positive $T\Delta S^{noncomb}$, we consider the entropy gain of breaking a hydrogen bond of $T\Delta S_{HB}$ ~ 6 kJ • mol^{-1} (72) and the entropy gain associated with the release of a single water molecule from a hydrated surface of ~ 7.5 kJ • mol^{-1} (75). Given that our FTS study only considered excess ions, but no counterions, while fully capturing the LCST behavior through the excluded volume, *v*, our results are consistent with the hypothesis that competing hydrophilic/hydrophobic interactions are responsible for the LCST behavior (76–78). At low temperatures, the attractive interaction between water and hydrophilic residues of the biopolymer stabilize the homogenous phase, but above a critical temperature hydrophobic interactions become dominant, in that it becomes more favorable for water to be released from the polymer surface and hydration shell, and for tau and RNA to associate. In this scenario, the entropy gain comes from the release of bound water into the bulk [70] due to overlapping of the hydration shell of tau upon CC. In the literature, the entropy gain of counter ion release (79–82) or compressibility effects (83,84) have been

558 proposed as origins for the LCST behavior, and as prevalent driving forces for CC (85). While
559 this study cannot entirely delineate between these possible contributions that are all subsumed
560 into the Flory-Huggins χ parameter or the excluded volume parameter in FTS, we demonstrate
561 that it is not necessary to invoke a specific mechanism, such as counter ion release—the most
562 popular hypothesis, to rationalize LCST driven CC formation. In fact, we performed FTS studies
563 with (and without) explicit excess ions (Fig. 6C) observing LCST behavior simply by means of
564 excluded volume and electrostatic considerations and not invoking any counter ion release
565 mechanism to capture the phase diagram of the entropy driven tau-RNA CC. Instead, many
566 factors that globally modulate the excluded volume effects in the biological system of interest
567 and that inevitably modulate the hydration water population, including the hydrophobic effect
568 and crowding, may be considered.

569 We demonstrated here that tau-RNA CC can be modeled as a coarse-grained
570 polyelectrolyte mixture using equilibrium theory, and revealed the associated driving factors and
571 the different thermodynamic contributions to the phase diagram. However, this finding does not
572 contradict the possibility that tau-RNA complex coacervation is followed by, or even can
573 facilitate, amyloid fibrillization of tau. Comparing our study to previous reports in the literature
574 (21–23,25,86,87), it is clear that tau in fibrils possess dramatically different properties than tau in
575 CCs. In contrast to fibrils, tau-RNA CCs are reversible and tau remains conformationally
576 dynamic – this is because CCs are formed with a stable tau variant, such as the WT derived tau
577 studied here. However, once aggregation-promoting factors are introduced, not only can the
578 thermodynamically stable phase of tau-RNA CC be driven out of equilibrium, but the dense CC
579 phase harboring high tau and RNA concentration may also lower the activation barrier for, and
580 thus facilitate, tau aggregation. Still, tau complex coacervation is a distinct state and fibrilization

581 is a distinct process, where the equilibrium of one does not contradict with its kinetic
582 transformation into the other. Recently, the possibility of the transformation of tau CCs into tau
583 fibrils has been demonstrated (21). We have independently investigated these questions and find
584 that irreversible transformation can be triggered by doping tau-RNA CC with highly sulfated
585 polysaccharide heparin (Fig. S9). Tau is first driven towards an equilibrium complex coacervate
586 state, from which tau can either re-dissolve into solution state reversibly, or form amyloid fibrils
587 when aggregation driving force is present. However, the mechanism by which the CC state of tau
588 influences the rate of aggregation and/or alters the aggregation propensity of tau is not
589 understood, and will and should be the subject of future studies.

590 The physiological role of tau-RNA CC as a possible regulatory mechanism or as an
591 intermediate toward fibrilization is an ongoing topic of research. In either case, for tau-RNA CC
592 to be relevant for cellular function LLPS would have to be possible near (certain) physiological
593 conditions. Our *in vitro* experiments found the tau-RNA CC phase diagram boundary to lie near
594 physiological conditions. This suggests that tau-RNA CC can occur *in vivo* upon modulation of
595 parameters, such as the local temperature, electrostatic balance, including local pH, and osmotic
596 pressure. We demonstrate that indeed tau-RNA CC can be achieved in co-culture with living
597 cells. While the coexistence of tau and RNA at low (10 μM) polymer concentrations is not
598 sufficient to drive CC in cellular media, the addition of a molecular crowding reagent is, under
599 physiological conditions (Fig. 7). While in this study crowding has been simulated with PEG,
600 many cellular proteins can act as molecular crowding reagents. This data encourages us to
601 speculate that mechanisms that increase the already high concentrations of free proteins and
602 other macromolecular constituents, *not* participating in CC, beyond the normal level within the
603 cell (estimates of 50-200 mg/mL (88)) could be sufficient to promote tau-RNA CC by exerting

crowding pressure. Thus, biological mechanisms that increase the concentration of intrinsically disordered and charged proteins and nucleic acids may be potent factors that drive liquid-liquid phase separation in the cellular context. Specifically for the context of this study, high concentrations of tau-RNA are by themselves sufficient to drive CC formation (Fig. 7). Given that tau is known to bind and localize to microtubules in the axons of neurons, it is not a stretch to envision a scenario where the local concentration of tau would be highly elevated under certain stress conditions, around regions like the axon initial segment. We proposed at these places in neuron, tau-RNA CCs have a higher probability to be observed. However, even though our calculations and experimental data support a model where tau-RNA CC *in vivo* is possible, whether this actually occurs within the cell depends on many other factors, among them the strength of tau-microtubule binding that compete with tau-RNA CC.

Conclusion

We report here the first detailed picture of the thermodynamics of tau/RNA complex coacervation. The observation of an LCST phase diagram implies that although electrostatic interactions are key to CC formation, factors that contribute to solvation entropy gain are key to driving liquid-liquid phase separation. We have computed the first approximation-free theoretical phase diagram for tau/RNA complex coacervation from FTS, where we introduced a temperature-dependent excluded volume term. Simulations show a competition between electrostatic strength (parameterized by the salt concentration) and excluded volume (parameterized by the solvent quality). This knowledge can be used to design experiments that perturb this parameter space *in vivo*, as well as predict or understand biological mechanisms that

may be favorable towards liquid-liquid phase separation. As a proof of this concept we have shown that by deliberately changing salt concentration, temperature, and solvent quality (by the addition of PEG), we can make tau/RNA LLPS appear or disappear in cellular medium with *live* cells. Interestingly, we find that without any adjustable parameters our simulations predict that tau/RNA is positioned near the binodal phase boundary around physiological conditions. This suggests that small and subtle changes within the cellular environment may be sufficient to induce LLPS in otherwise healthy neurons. Even if the conditions that induce LLPS in the cell is transient, the LLPS state can facilitate irreversible protein aggregation if aggregation-promoting factors are already available, giving credence to the idea that LLPS may play a role in neurodegenerative diseases. However, we speculate that LLPS is reversible in the majority of biological events that drive LLPS, making it hard to observe this state within the cellular context.

Materials and Methods

Protein expression and purification

Unless stated, a 20 mM ammonium acetate buffer at pH 7.0 was used and referred to here as final buffer. Tau, RNA, NaCl, PEG and other stocks were prepared using final buffer. Measurements were taken in final buffer at room temperature unless stated.

N-terminal truncated, microtubule binding domain containing tau187 (residues 255-441 with a His-tag at the N-terminus) were used for *in vitro* studies. The cloning, expression, and purification have been previously described (57,89). The single cysteine variant of tau187 (tau187C291S) were generated via site-direct mutagenesis. E. coli BL21 (DE3) cells previously transfected were cultured from frozen glycerol stock overnight in 10 mL luria broth (LB) which

was used to inoculate 1 L of fresh LB. Culturing and inoculation were performed at 37 °C with shaking of 200 rpm. At OD_{600} of 0.6–0.8, tau187 variant expression was induced by incubation with 1 mM isopropylß-D-thiogalactoside (Sigma Aldrich) for 2–3 h. Cells were harvested by centrifugation for 30 min at 5000 × g (Beckman J-10; Beckman Instruments, Inc.), and the pellets were stored at −20 °C until further use.

Cell pellets were resuspended in lysis buffer (Tris-HCl pH 7.4, 100 mM NaCl, 0.5 mM DTT, 0.1 mM EDTA, 1mM PMSF) with 1 Pierce protease inhibitor tablet (Thermo Fisher). Lysis was initiated by the addition of lysozyme (2 mg/ml), DNase (20 µg/ml), and $MgCl_2$ (10 mM) and incubated for 30 min on ice. Lysate was then heated to 65 °C for 13 min, cooled on ice for 20 min and then centrifuged to remove the precipitant. The supernatant was loaded onto a Ni-NTA agarose column pre-equilibrated with wash buffer A (20 mM sodium phosphate pH 7.0, 500 mM NaCl, 10 mM imidazole, 100 µM EDTA). The column was then washed with 20 ml of buffer A, 15 ml buffer B (20 mM sodium phosphate pH 7.0, 1 M NaCl, 20 mM imidazole, 0.5 mM DTT, 100 µM EDTA). Purified tau187 was eluted with buffer C (20 mM sodium phosphate pH 7.0, 0.5 mM DTT, 100 mM NaCl) supplemented with varying amounts of imidazole increasing from 100 mM to 300 mM. The protein was then concentrated via centrifugal filters (MWCO 10 kDa; Millipore Sigma) and the buffer was exchanged into final buffer by PD-10 desalting column (GE Healthcare). The final protein concentration was determined by UV-Vis absorption at 274 nm using an extinction coefficient of 2.8 $cm^{-1}mM^{-1}$, calculated from absorption of Tyrosine [3].

Spin labeling and cw EPR

Freshly eluted tau187C291S (with one cysteine at site 322) was replaced in final buffer using a PD-10 desalting column (GE Healthcare). Protein after PD-10 was labeled overnight at 4°C by immediately mixing with a 10-fold molar excess of the spin label (1-oxyl-2,2,5,5-

673 tetramethylpyrroline-3-methyl) methanethiosulfonate (MTSL; Toronto Research Chemicals),
674 resulting in spin labelled tau (tau187C291S-SL). Excess label was removed using PD-10. The
675 protein was concentrated using centrifugal filter (MWCO 10 kDa; Amicon) and the final protein
676 concentration was determined by UV-Vis absorption at 274 nm as mentioned above. Non-
677 labeled tau187C291S was used in order to achieve spin dilution.
678 Cw EPR measurements were carried out using a X-band spectrometer operating at 9.8 GHz
679 (EMX; Bruker Biospin, Billerica, MA) and a dielectric cavity (ER 4123D; Bruker Biospin,
680 Billerica, MA). 100 μM tau187C291S-SL was mixed with 400 μM tau187C291S to reach 20%
681 spin labeling. Samples under droplet forming condition were prepared by adding 1.5 mg/ml
682 RNA, and tau samples under aggregation-inducing conditions prepared by adding 125 μM
683 heparin (15 kDa average MW; Sigma-Aldrich). A sample of 4.0 μl volume was loaded into a
684 quartz capillary (CV6084; VitroCom) and sealed at both ends with critoseal, and then placed in
685 the dielectric cavity for measurements. Cw EPR spectra were acquired by using 6 mW of
686 microwave power, 0.5 gauss modulation amplitude, 100 gauss sweep width, and 8-64 scans for
687 signal averaging.

688 **Cw EPR spectra analysis**

689 The recorded cw EPR spectra were subjected to single- or double-component simulation. EPR
690 simulation and fitting were performed using MultiComponent, a program developed by Christian
691 Altenbach (University of California, Los Angeles). For all spectra fitting, the magnetic tensors A
692 and g were fixed and used as constraints as previously reported (87). These values are A_{xx} = 6.2
693 G, A_{yy} = 5.9 G, A_{zz} = 37.0 G, and g_{xx} = 2.0078, g_{yy} = 2.0058, and g_{zz} = 2.0022.
694 For soluble tau, the cw EPR spectra were best fitted with a single-component simulation and the
695 rotational diffusion constant (R) can be extracted. The rotation correlation time τ_R was calculated

using $\tau_R = 1/(6R)$. For tau-heparin aggregates, the cw EPR were subjected to double-component simulation, where the parameters of the fitted single-component were used as a mobile-component. The immobile-component were set to be identical to the mobile-component, except the diffusion tensor tilt angle $\beta_D = 36°$ and the order parameter S. The fitting parameters were limited at a minimum, which includes the population, p, rotational diffusion constants of mobile- and immobile-component, R_1 and R_2, and the order paramter, S of the immobile-component. The fitted immobile-component were used to represent the rotational correlation time for tau-heparin fibrils. For tau-RNA CC. the cw EPR spectra were subjected to both single- and double-component fitting. Comparing the two fitting schemes showed that singl-component fitting has almost overlapped the cw EPR spectra, while double-component fitting results in a immobile-component population of ~10% (data not shown). This showed that tau-RNA CC cw EPR spectra can be sufficiently fit with single-component. The fitted rotational correlation time was calculated and plotted against tau-heparin samples.

Turbidimetry and brightfield microscopy

Turbidity of samples at room temperature were represented by optical density at a 500-nm wavelength (OD_{500}), using a Shimadzu UV-1601 spectrophotometer (Shimadzu Inc.). The amount of coacervates in a sample were approximated to be propotional to its OD_{500}.

Tubidity of samples at ramping temperatures were represented by OD_{500} measured using Jasco J-1500 CD Spectrometer (JASCO Inc.) equipped with temperature controller and spectrophotometer. 120 µL of 20 µM tau187C291S, 60 µg/mL polyU RNA and 30 mM NaCl in working buffer were prepared in a 100 µL cuvette (Starna Scientific Ltd) and kept at 4 °C for 5 min before cycling. Heating and cooling temperatures were ramped at 1 °C/min while OD_{500} was monitored.

Bright field images were examed to confirm the presence of tau-RNA CC. 100 μM tau187C291S and 300 μg/mL polyU RNA was mixed in presence of 20 mM ammonium acetate and 30 mM NaCl. 10 μl of the mixture was pipetted onto a microscope slide with a cover slide gapped by two layers of double-sided sticky tape. Temperatures were controlled using an incubator. Bright field images were acquired using a spectral confocal microscope (Olympus Fluoview 1000; Olympus, Center Valley, PA).

Determining tau-RNA CC composition

It was shown by fluorescence microscopy in protein-RNA LLPS that protein is concentrated inside the droplet (14,90). For representing tau inside the droplets with measurement taken from droplet suspension, we quantified the percentage of tau present as droplets. After mixing and centrifuging 60 μL droplet suspension of 400 μM tau187/322C and 1500 μg/mL polyU, ~1 μL dense phase was generated with clear boundary against dilute phase. Dissolving dense phase in high concentration of NaCl resulted in transparent solution thus UV absorption can be measured. Due to the difficulty of preparing large volume of pure dense phase, we can only underestimate the tau and polyU concentration in dense phase. Since tau and RNA have different UV absorbance spectra, fitting spectra of the tau-RNA mixed sample with those of pure tau and polyU generated the concentration of both. Fitting results showed that over 99% of the tau and over 99.9% of polyU were condensed inside the dense phase. This partitioning guaranteed that the property of tau in the droplet suspension represents those in the droplets.

Cell Culture and confocal microscopy

Protein (tau187 or K18) was labeled with Alexa Fluor® 488 or 555 5-SDP ester (Life Technologies) according to the suppliers instructions. After labeling, 100 mM glycine was added to quench the reaction and the proteins were subjected to Zeba desalting columns (Thermo

Scientific) to remove any unreacted label. Average label incorporation was between 1 and 1.5 moles/mole of protein, as determined by measuring fluorescence and protein concentration (A_{max} $\times$MW of protein / [protein]$\times\varepsilon_{dye}$).

H4 neuroglioma cells (ATCC® HTB-148) were cultured in DMEM supplemented with 10% FBS, 100 μg/ml penicillin/streptomycin. Cultures were maintained in a humidified atmosphere of 5% CO_2 at 37°C. Tau protein (1:20 labeled K18:unlabeled tau114), RNA, PEG, and media (DMEM,10% FBS,1% Pen/Strep) were mixed at the indicated concentrations and added to cells at varying temperatures. Images were obtained on a Leica SP8 Resonant Scanning Confocal.

Tau *in vitro* Phosphorylation

Phosphorylation of tau was performed as previously described (Despres, C et. al PNAS 2017). In brief, tau protein (40uL at 6mM) was mixed with 200 μL mouse brain extract and incubated overnight at 37 °C in phosphorylation buffer (40 mM HEPES pH 7.3, 2 mM $MgCl_2$, 5 mM EGTA, 2 mM DTT, 2 mM ATP, 1 μM okadaic acid, protease inhibitors). After incubation, samples were centrifuged and the supernatant was buffer exchanged using zeba desalting columns (Thermo Fisher) into buffer (20 mM ammonium acetate, pH 7). Concentration was determined by BCA assay. Phosphorylation was confirmed using a western blot assay to look at phospho-epitopes 396/404 using PHF-1 Antibody (Peter Davies).

Flory-Huggins based Voorn-Overbeek (FH-VO) modeling

FH-VO is based on a Flory-Huggins (FH) treatment, where the polymer system is mapped onto a lattice. Voorn and Overbeek extended the FH formalism to polyelectrolytes by including long-ranged electrostatic interactions with a Debye–Hückel term. The resulting expression for the free energy of mixing (ΔGmix) per lattice site is

$$\frac{\Delta G_m}{M k_B T} = \sum \frac{\phi_i}{N_i} ln\phi_i - \alpha[\sum \sigma_i \phi_i]^{\frac{3}{2}} + \sum \chi_{ij} \phi_i \phi_j \qquad \text{(S1)}$$

765 Where $M = V/(l_w)^3$ is the total number of lattice sites. In Eqn.S1, the index i refers to one of
766 the five species. N_i is the degree of polymerization for species i. For tau187 and tau114, N_i
767 equals to the length of the polypeptides (Table S1); while for RNA, N_i is estimated by the
768 average MW 900 kDa for polyU RNA and the MW of condensated uridine monophosphate, 306
769 Da. For monovalent ions and water, $N_i = 1$.
770 σ_i is the average charge per monomer, which is determined by (net charge) / N_i. The net charges
771 of tau at experimental pH conditions (pH = 7) were estimated based on primary sequences in
772 Table S1, using pepcalc.com. σ_i for other species were listed in Table S2. In FH-VO model, σ_i is
773 fixed. We also consider a modified version, a FH-VO-CR model, where σ_i of RNA is set to a
774 function of temperature as discussed further below.
775 In Eqn. S1, ϕ_i is the volume fraction of species (tau, RNA, Na^+, Cl^-, H_2O). ϕ_i was computed by
776 $\phi_i = c_i \times N_i \times \frac{1}{c_w}$ where c_i is the molar concentration and c_w the molar concentration of pure water
777 computed from water volume molarity: c_w = 55.56 mol/L. In experiments, c_{tau} and c_{RNA} were
778 designed to reach a 1:1 charge ratio, therefore, we have $N_{RNA} \times c_{RNA} = 11 \times c_{tau} = 11 \times [tau]$. In
779 addition to NaCl, there is 20 mM ammonium acetate in the buffer. The total monovalent salt
780 concentration is $c_{salt} = c_{NaCl} + 20\ mM = [NaCl] + 20\ mM$. Therefore, ϕ_i were calculated from
781 experimental [tau] and [NaCl] as,

$$\begin{aligned} \phi_{tau} &= [tau] \times 207 \times \frac{1}{c_w} \\ \phi_{RNA} &= [tau] \times 11 \times \frac{1}{c_w} \\ \phi_{salt} &= ([NaCl] + 20\ mM) \times \frac{1}{c_w} \\ \phi_{polymer} &= \phi_{tau} + \phi_{RNA} = [tau] \times 218 \times \frac{1}{c_w} \end{aligned} \tag{S2}$$

$$\phi_{water} = 1 - \phi_{polymer} - \phi_{salt}$$

782

783 α is the strength of the electrostatic interactions defined as

$$\alpha = \frac{2}{3}\sqrt{\frac{\pi}{l_w^3}}\left(\frac{e^2}{4\pi\epsilon_r\epsilon_0 k_B T}\right)^{3/2} \quad \text{(S3)}$$

784 where l_w is the length of a lattice, computed from c_w, $l_w = \sqrt[3]{\frac{1\times10^{-3}m^3}{c_w N_A}}$, $\epsilon_r\epsilon_0$ the water permitivity,

785 $\epsilon_r\epsilon_0 = 80\times8.85\times10^{-12}\ F/m$, k_B the Boltzmann constant and T the absolute temperature.

786 χ_{ij} is the Flory-Huggins interaction parameter between species i and j, which will be defined and

787 descussed below.

788 The three terms on the right-hand side of Eqn. S1 are respectively: 1) the ideal Flory-Huggins

789 mixing entropy, 2) the mixing enthalpy due to Coulombic interactions based on Debye–Hückel

790 approximation (91) and 3) the excess free energy to account for the non-Coulombic interactions,

791 which can include contributions from water perturbation (92), cation-π interaction (93) and

792 dipole-dipole interactions (94). Eqn. S1 has been successfully applied in PDMAEMA-PAA

793 complex coacervate (29). In this work we refer to Eqn. S1 as FH-VO model, which is a minimal

794 model for complex coacervation.

795 **Determining phase separation temperature**

796 A phase separation temperature, T_{cp}, was assigned to the cloud point of the sample. T_{cp} was

797 determined by fitting normalized turbidity-temperature curves to a sigmoid function as follows

799 $$normalized\ turbidity = \frac{1}{1 + exp\left(-k\times\left(T - T_{cp}\right)\right)},$$

798 to find

$$T = T_{cp}.$$

FH-VO bindal curve computation

ϕ_i and T can be converted from/to experimental conditions as described, where tau and RNA are added at a fixed charge neutrality ratio. Therefore, ΔG_{mix} depends on four variables: total polymer volume fraction $\phi_{polymer} = \phi_p + \phi_q$, total salt volume fraction $\phi_{salt} = \phi_{s+} + \phi_{s-}$, temperature T and X, a matrix of $\chi_{pp}, \chi_{pq}, \chi_{ps+}, \dots, \chi_{qp}, \chi_{qq}, \dots$. A two-phase equilibrium exists where the sum of mixing free energy of two coexisting phases are lower than that of the homogeneous mixture. For simplicity, we adopt the assumption that the salt concentration in both two phases are identical (29), leaving the system a binary mixture of polymer and buffer. Binodal compositions are defined by pairs of points on the curve of ΔG_{mixing} vs. $\phi_{polymer}$ that have common tangents, corresponding to compositions of equal chemical potentials of both buffer and polymer in dense and dilute phases.

A binodal composition curve (binodal curve) was computed by finding the bi-tangent points of ΔG_{mixing} vs. $\phi_{polymer}$ at a series of ϕ_{salt} at given temperature T and given parameters. Given ϕ_{salt}, T and X, the mixing free energy is solely dependent on $\phi = \phi_{polymer}$:

$$f(\phi) = \Delta G_{mixing}(\phi_{polymer})$$

A bi-tangent pair (ϕ_1, f_1), (ϕ_2, f_2) was calculated by solving the set of nonlinear equations (67,95),

$$\begin{cases} \left.\frac{\partial f}{\partial \phi}\right|_{\phi=\phi_1} - \left.\frac{\partial f}{\partial \phi}\right|_{\phi=\phi_2} = 0 \\ \left.\left(f - \phi\frac{\partial f}{\partial \phi}\right)\right|_{\phi=\phi_1} - \left.\left(f - \phi\frac{\partial f}{\partial \phi}\right)\right|_{\phi=\phi_2} = 0 \end{cases}$$

which was solved by R function *nleqslv* using Newton-Ralphson algorithm at given initial guess. Finally, the $\phi_{polymer}$ and ϕ_{salt} were converted into [tau] and [NaCl] as described.

Coarse grained polyelectrolyte model used in FTS

Our system consists of n total polymers made up of n_τ tau molecules of length N_τ and n_p RNA molecules of length N_p. Each amino acid is treated as a single Kuhn segment of length b. The solvent is treated implicitly with a uniform dielectric background ϵ. For simplicity we only consider the symmetric case of $N_p = N_\tau$. Chain connectivity is enforced by a harmonic bond potential of the form $\beta U_{bond} = \frac{3}{2b^2}\sum_{\alpha=1}^{n}\sum_{j=1}^{N}(|\boldsymbol{r}_{\alpha,j} - \boldsymbol{r}_{\alpha,j-1}|)^2$ where $\boldsymbol{r}_{\alpha,j}$ is the coordinates of bead j on chain α. In addition to chain connectivity, all monomers interact with a short-ranged excluded volume potential (65). We take the well-known Edward's delta function model for the excluded volume interaction $\beta U_{ex} = v\delta(\boldsymbol{r})$ where v is the excluded volume parameter (65). The charge of each bead j for the tau molecule $z_{\tau,j}$ is determined from the primary amino acid sequence with aspartic (D) and glutamic (E) acid being $z_{\tau,j} = -1$, arginine (R) and lysine (K) being $z_{\tau,j} = +1$ and all other amino acids being neutral $z_{\tau,j} = 0$. The RNA chain is treated as a fully-charged chain with $z_{p,j} = -1$ for all monomers. Charged segments interact via a long-ranged Coulomb potential $\beta U_{el} = \frac{l_B z_i z_j}{r}$ with $l_B = \frac{e^2}{4\pi\epsilon_0\epsilon_r k_B T}$ being the Bjerrum length, e is the unit of electronic charge, ϵ_0 is the vacuum permittivity, and ϵ_r is the dielectric constant. For a schematic depiction of the polymer physics model see Fig. 3 in the main text.

The model is ``regularized" by smearing all statistical segments over a finite volume instead of treating them as point particles (96). This is accomplished by endowing each bead with a Gaussian profile with a width on the order of the statistical segment length $\Gamma(r) = (3/\pi b^2)^2 \exp(-3r^2/b^2)$ where r is a radial distance from the monomer center. As a consequence of this density smearing, the interactions between monomers ``softens" (97).

Transformation of particle model to a statistical field theory

The advantage of the coarse-grained polyelectrolyte model employed in this work is that it can be exactly converted to a statistical field theory by utilizing a Hubbard-Stratonovich transformation as described in (98). Invoking this transformation, the canonical partition function is expressed in terms of two fluctuating auxiliary fields w and φ which serve to decouple the excluded volume and Coulombic interactions respectively [14], [16]–[19]. In the statistical field representations the canonical partition function is

$$Z = Z_0 \int Dw \int D\varphi \exp\left(-H[w,\varphi]\right) \qquad \text{(S4)}$$

where Z_0 contains the ideal gas partition function and self-interaction terms. The field-theoretic Hamiltonian for this model is

$$H[w,\varphi] = \frac{1}{2v}\int d\boldsymbol{r}\, w(\boldsymbol{r})^2 + \frac{1}{8\pi l_B}\int d\boldsymbol{r}\, |\nabla\varphi|^2 - n_\tau \ln\, Q_\tau\,[w,\varphi] - n_p \ln\, Q_p[w,\varphi] \quad \text{(S5)}$$

where $Q_\tau[w,\varphi]$ and $Q_p[w,\varphi]$ are the partition functions for a single tau and a single RNA molecule in the conjugate fields. These single chain partition functions can be computed using a Gaussian chain propagator such that

$$Q_l[\psi] = \frac{1}{V}\int d\boldsymbol{r}\, q_l(\boldsymbol{r}, N_l; \psi) \quad \text{(S6)}$$

where l indexes the chain type (tau/RNA) and $\psi(j) = i\,\Gamma \star \left(w + z_j\varphi\right)$ with $i = \sqrt{-1}$ and $\star$ a spatial convolution. The chain propagator $q_l(\boldsymbol{r}, j; \psi)$ is constructed from a Chapman-Kolmogorov-type equation

$$q_l(\boldsymbol{r}, j+1; \psi) = \left(\frac{3}{2\pi b^2}\right)^{3/2} \exp\left[-\psi(\boldsymbol{r}, j+1)\right] \int d\boldsymbol{r}'\, q_l(\boldsymbol{r}', j; \psi) exp\left(-\frac{3|\boldsymbol{r}-\boldsymbol{r}'|^2}{2b^2}\right) \quad \text{(S7)}$$

with initial condition $q_l(\boldsymbol{r}, 0; \psi) = \exp[-\psi(\boldsymbol{r}, 0)]$. From the field theoretic Hamiltonian any thermodynamic observable may be computed as an ensemble average of a corresponding operator expressed in terms of the field configurations $\widetilde{G}[w, \varphi]$

$$\langle G \rangle = \frac{Z_0}{Z} \int Dw \int D\varphi \, \widetilde{G}[w, \varphi] \exp(-H[w, \varphi]) \quad \text{(S8)}$$

We stress that no additional approximations are made in moving from a particle-based model to a statistical field theory. The advantage of such a transformation is that the pairwise interactions between monomers are decoupled in favor of interactions between monomers and a complex-valued field. This transformation is particularly suited to our purposes here as conventional particle simulations can only study the earliest stages of protein aggregation.

Field theoretic simulations using CL sampling

Field theoretic simulation (FTS) allows one to numerically compute ensemble averages of the form of Equation S8 by sampling along a stationary stochastic trajectory in the space of the field variables. The method has been presented in detail elsewhere (96,98,99). We use complex Langevin (CL) sampling (100,101) to stochastically sample the auxiliary fields. The method involves promoting the fields to be complex-valued and numerically propagating the CL equations of motion

$$\begin{aligned} \frac{\partial w(\boldsymbol{r},t)}{\partial t} &= -\lambda_w \frac{\delta H[w,\varphi]}{\delta w(\boldsymbol{r},t)} + \eta_w(\boldsymbol{r}, t) \\ \frac{\partial \varphi(\boldsymbol{r},t)}{\partial t} &= -\lambda_\varphi \frac{\delta H[w,\varphi]}{\delta \varphi(\boldsymbol{r},t)} + \eta_\varphi(\boldsymbol{r}, t) \end{aligned} \quad \text{(S9)}$$

where $\eta_w(\boldsymbol{r}, t)$ and $\eta_\varphi(\boldsymbol{r}, t)$ are real-valued Gaussian white-noise random variables with zero mean and variance proportional to the dissipative coefficients λ_w and λ_φ. A single FTS step involves computing the single chain partition functions for a given field configurations (w, φ) given by Equation S6 along with any operators $\widetilde{G}[w, \varphi]$ followed by updating the field configurations according to Equation S9. Under the condition that the system is ergotic,

ensemble averages are computed as time averages over the CL trajectory. All FTS-CL simulations were performed in reduced units by scaling spatial lengths by a reference distance $R_0 = b/\sqrt{6}$ corresponding to the prefactor in the scaling relation of an ideal homopolymer radius of gyration with respect to the chain length $R_g = R_0 N^{1/2}$ (102). Simulations were performed in a cubic box of length $L = 34.0\ R_0$ using periodic boundary conditions. Fields were sampled with a spatial collocation mesh of 32^3 sites. An exponential time difference (ETD) algorithm (103,104) with $\Delta t = 0.01$ was used to numerically propagate the CL equations of motion Equation S13. All simulations were performed on NVIDIA Tesla M2070 or K80 graphics processing units (GPUs).

The thermodynamic state of the system is fully determined by specifying a dimensionless excluded volume parameter $B = v/{R_0}^3$, a dimensionless Bjerrum length $E = 4\pi l_B/R_0$, and a dimensionless polymer chain number density $C = \rho R_0^3$ with $\rho = \sum_l n_l N_l /V$ where l indexes the chain type (tau or RNA). Additionally, we require the fraction of chains of each type $\phi_l = n_l N_l / \sum_l n_l N_l$. In this work we consider only a 1:1 charge ratio, which for the model shown in Fig. 1 corresponds to $\phi_\tau = 0.954$ and $\phi_p = 0.046$.

Determination of phase equilibria from FTS

In order to compute the phase coexistence points from FTS we need to compute the chemical potential μ and the osmotic pressure Π. The chemical potential operator for chain type l is $\tilde{\mu}_l = \ln \frac{\rho {R_0}^3 \overline{\phi_l}}{N_l} - \ln Q_l$. For the pressure operator we use the form given in Appendix B of (55). The conditions for the stable coexistence of two phases is given by the chemical equilibrium condition $\sum_l \nu_l {\mu_l}^I = \sum_l \nu_l {\mu_l}^{II}$ and the mechanical equilibrium condition $\Pi^I = \Pi^{II}$. The stoichiometric coefficient ν_l ensures charge neutrality. The procedure we employ in this work is

that of (55), and involves computing the chemical potential and pressure for a range of polymer concentrations. Fig. S7 (Left) shows a plot of the osmotic pressure vs. the chemical potential for different polymer conentrations. The simulation data represent three branches: a dilute branch (red), a conentrated branch (blue), and an unstable branch (orange). The equilibrium condition of equal chemical potential and equal osmotic pressure can be directly gleaned from the intersection of the dilute and concentrated branch. This gives the critical conditions for phase coexistence. Fig. S7 (Right) show a plot of the chemical potential vs. polymer concentration. The critical chemical potential value is shown by the dashed horizontal line. The intersection of this line with the polymer concentration data points from FTS gives the dilute supernatant polymer concetration ρ^{I} and the coacervate concentration of the coexisting phase ρ^{II}. By repeating this procedure for many different thermodynamic conditions we can construct the phase diagrams shown in Fig. 5 of the main text.

Calculation of non-ionic entropy and enthalpy of coacervation

As discussed in the main text the interaction parameter is decomposed into an entropic and enthalpic contribution $\chi = \epsilon_s + \epsilon_H/T$. According to the Flory-Huggins treatment the non-combinatoric contribution to the Gibbs free energy of mixing is

$$\Delta G_{mix} = \mathrm{RTn}_p \chi \phi_w$$

where R is the ideal gas constant, T is the temperature, n_p is the total number of moles of monomer units, and ϕ_w is the volume fraction of water. From the relation $\Delta S_{mix} = -\frac{\partial \Delta G_{mix}}{\partial T}$, the non-ideal entropy of mixing is

$$\Delta S_{mix} = -\mathrm{Rn}_p \phi_w \epsilon_s.$$

From the relation $\Delta H_{mix} = \Delta G_{mix} + T\Delta S_{mix}$, the enthalpy of mixing arising from non-ionic interactions is

927 $$\Delta H_{mix} = \mathrm{Rn}_p \phi_w \epsilon_H.$$

928 Values in the main text are computed using a water volume fraction of $\phi_w = 0.722$. See Table
929 S3 for further details.

930

931 # Acknowledgements

932 We acknowledge insightful and sustained discussions with Dr. Xumei Zhang on LLPS of tau
933 under cellular conditions. JM would like to thank Scott P.O. Danielsen for helpful discussions
934 regarding FTS. We acknowledge the use of the NRI-MCDB Microscopy Facility at UC, Santa
935 Barbara.

REFERENCE

1. Burke KA, Janke AM, Rhine CL, Fawzi NL. Residue-by-Residue View of In Vitro FUS Granules that Bind the C-Terminal Domain of RNA Polymerase II. Mol Cell. 2015 Oct 15;60(2):231–41.

2. Brady JP, Farber PJ, Sekhar A, Lin Y-H, Huang R, Bah A, et al. Structural and hydrodynamic properties of an intrinsically disordered region of a germ cell-specific protein on phase separation. Proc Natl Acad Sci. 2017 Sep 26;114(39):E8194–203.

3. Anderson P, Kedersha N. RNA granules. J Cell Biol. 2006 Mar 13;172(6):803–8.

4. Brangwynne CP, Eckmann CR, Courson DS, Rybarska A, Hoege C, Gharakhani J, et al. Germline P granules are liquid droplets that localize by controlled dissolution/condensation. Science. 2009 Jun 26;324(5935):1729–32.

5. Wippich F, Bodenmiller B, Trajkovska MG, Wanka S, Aebersold R, Pelkmans L. Dual specificity kinase DYRK3 couples stress granule condensation/dissolution to mTORC1 signaling. Cell. 2013 Feb 14;152(4):791–805.

6. Veis A, Aranyi C. Phase separation in polyelectrolyte systems. I. Complex coacervates of gelatin. J Phys Chem. 1960;64(9):1203–1210.

7. Arneodo C, Baszkin A, Benoit J, Thies C. Interfacial-Tension Behavior of Citrus Oils Against Phases Formed by Complex Coacervation of Gelatin. Acs Symp Ser. 1988;370:132–47.

8. Water JJ, Schack MM, Velazquez-Campoy A, Maltesen MJ, van de Weert M, Jorgensen L. Complex coacervates of hyaluronic acid and lysozyme: Effect on protein structure and physical stability. Eur J Pharm Biopharm. 2014 Oct;88(2):325–31.

9. Molliex A, Temirov J, Lee J, Coughlin M, Kanagaraj AP, Kim HJ, et al. Phase Separation by Low Complexity Domains Promotes Stress Granule Assembly and Drives Pathological Fibrillization. Cell. 2015 Sep;163(1):123–33.

10. Hyman AA, Weber CA, Jülicher F. Liquid-Liquid Phase Separation in Biology. Annu Rev Cell Dev Biol. 2014;30(1):39–58.

11. Uversky VN, Kuznetsova IM, Turoverov KK, Zaslavsky B. Intrinsically disordered proteins as crucial constituents of cellular aqueous two phase systems and coacervates. FEBS Lett. 2015 Jan 2;589(1):15–22.

12. Li YR, King OD, Shorter J, Gitler AD. Stress granules as crucibles of ALS pathogenesis. J Cell Biol. 2013 Apr 29;201(3):361–72.

13. Murakami T, Qamar S, Lin JQ, Schierle GSK, Rees E, Miyashita A, et al. ALS/FTD Mutation-Induced Phase Transition of FUS Liquid Droplets and Reversible Hydrogels into

970 Irreversible Hydrogels Impairs RNP Granule Function. Neuron. 2015 Nov 18;88(4):678–
971 90.

972 14. Patel A, Lee HO, Jawerth L, Maharana S, Jahnel M, Hein MY, et al. A Liquid-to-Solid
973 Phase Transition of the ALS Protein FUS Accelerated by Disease Mutation. Cell. 2015
974 Aug 27;162(5):1066–77.

975 15. Kato M, Han TW, Xie S, Shi K, Du X, Wu LC, et al. Cell-free formation of RNA
976 granules: low complexity sequence domains form dynamic fibers within hydrogels. Cell.
977 2012 May 11;149(4):753–67.

978 16. Li H-R, Chiang W-C, Chou P-C, Wang W-J, Huang J. TAR DNA-binding protein 43
979 (TDP-43) liquid-liquid phase separation is mediated by just a few aromatic residues. J Biol
980 Chem. 2018 Mar 6;jbc.AC117.001037.

981 17. Kwon I, Xiang S, Kato M, Wu L, Theodoropoulos P, Wang T, et al. Poly-dipeptides
982 encoded by the C9orf72 repeats bind nucleoli, impede RNA biogenesis, and kill cells.
983 Science. 2014 Sep 5;345(6201):1139–45.

984 18. Lee K-H, Zhang P, Kim HJ, Mitrea DM, Sarkar M, Freibaum BD, et al. C9orf72
985 Dipeptide Repeats Impair the Assembly, Dynamics, and Function of Membrane-Less
986 Organelles. Cell. 2016 Oct 20;167(3):774-788.e17.

987 19. Boeynaems S, Bogaert E, Kovacs D, Konijnenberg A, Timmerman E, Volkov A, et al.
988 Phase Separation of C9orf72 Dipeptide Repeats Perturbs Stress Granule Dynamics. Mol
989 Cell. 2017 Mar 16;65(6):1044-1055.e5.

990 20. Nott TJ, Petsalaki E, Farber P, Jervis D, Fussner E, Plochowietz A, et al. Phase Transition
991 of a Disordered Nuage Protein Generates Environmentally Responsive Membraneless
992 Organelles. Mol Cell. 2015 Mar 5;57(5):936–47.

993 21. Ambadipudi S, Biernat J, Riedel D, Mandelkow E, Zweckstetter M. Liquid–liquid phase
994 separation of the microtubule-binding repeats of the Alzheimer-related protein Tau. Nat
995 Commun. 2017 Aug 17;8(1):275.

996 22. Zhang X, Lin Y, Eschmann NA, Zhou H, Rauch JN, Hernandez I, et al. RNA stores tau
997 reversibly in complex coacervates. PLOS Biol. 2017 Jul 6;15(7):e2002183.

998 23. Hernández-Vega A, Braun M, Scharrel L, Jahnel M, Wegmann S, Hyman BT, et al. Local
999 Nucleation of Microtubule Bundles through Tubulin Concentration into a Condensed Tau
1000 Phase. Cell Rep. 2017 Sep 5;20(10):2304–12.

1001 24. Ferreon JC, Jain A, Choi K-J, Tsoi PS, MacKenzie KR, Jung SY, et al. Acetylation
1002 Disfavors Tau Phase Separation. Int J Mol Sci. 2018 May 4;19(5).

1003 25. Wegmann S, Eftekharzadeh B, Tepper K, Zoltowska KM, Bennett RE, Dujardin S, et al.
1004 Tau protein liquid-liquid phase separation can initiate tau aggregation. EMBO J. 2018 Apr
1005 3;37(7).

26. Bungenberg de Jong H. Crystallisation–coacervation–flocculation. Colloid Sci. 1949;2:232–58.

27. Sing CE. Development of the modern theory of polymeric complex coacervation. Adv Colloid Interface Sci. 2017 Jan;239:2–16.

28. Flory PJ. Principles of Polymer Chemistry [Internet]. 1953 [cited 2018 Jun 21]. Available from: http://archive.org/details/FloryF.1953PrinciplesOfPolymerChemistry

29. Spruijt E, Westphal AH, Borst JW, Cohen Stuart MA, van der Gucht J. Binodal Compositions of Polyelectrolyte Complexes. Macromolecules. 2010 Aug 10;43(15):6476–84.

30. Overbeek JTG, Voorn MJ. Phase separation in polyelectrolyte solutions. Theory of complex coacervation. J Cell Comp Physiol. 1957 May 1;49(S1):7–26.

31. Tainaka K. Study of Complex Coacervation in Low Concentration by Virial Expansion Method. I. Salt Free Systems. J Phys Soc Jpn. 1979 Jun 15;46(6):1899–906.

32. Veis A. PHASE SEPARATION IN POLYELECTROLYTE SYSTEMS. III. EFFECT OF AGGREGATION AND MOLECULAR WEIGHT HETEROGENEITY. J Phys Chem. 1963 Oct 1;67(10):1960–4.

33. Tainaka K-I. Effect of counterions on complex coacervation. Biopolymers. 1980 Jul 1;19(7):1289–98.

34. Nakajima A, Sato H. Phase relationships of an equivalent mixture of sulfated polyvinyl alcohol and aminoacetalyzed polyvinyl alcohol in microsalt aqueous solution. Biopolymers. 11(7):1345–55.

35. Borue VY, Erukhimovich IY. A statistical theory of weakly charged polyelectrolytes: fluctuations, equation of state and microphase separation. Macromolecules. 1988 Nov 1;21(11):3240–9.

36. Borue VY, Erukhimovich IY. A statistical theory of globular polyelectrolyte complexes. Macromolecules. 1990 Jul 1;23(15):3625–32.

37. Castelnovo M, Joanny J-F. Complexation between oppositely charged polyelectrolytes: Beyond the Random Phase Approximation. Eur Phys J E. 2001 Dec 1;6(1):377–86.

38. Biesheuvel PM, Cohen Stuart MA. Electrostatic Free Energy of Weakly Charged Macromolecules in Solution and Intermacromolecular Complexes Consisting of Oppositely Charged Polymers. Langmuir. 2004 Mar 1;20(7):2785–91.

39. Biesheuvel PM, Cohen Stuart MA. Cylindrical Cell Model for the Electrostatic Free Energy of Polyelectrolyte Complexes. Langmuir. 2004 May 1;20(11):4764–70.

40. Lytle TK, Sing CE. Transfer matrix theory of polymer complex coacervation. Soft Matter. 2017 Oct 11;13(39):7001–12.

41. Shen K, Wang Z-G. Polyelectrolyte Chain Structure and Solution Phase Behavior. Macromolecules. 2018 Mar 13;51(5):1706–17.

42. Shen K, Wang Z-G. Electrostatic correlations and the polyelectrolyte self energy. J Chem Phys. 2017 Feb 23;146(8):084901.

43. Chollakup R, Smitthipong W, Eisenbach CD, Tirrell M. Phase Behavior and Coacervation of Aqueous Poly(acrylic acid)−Poly(allylamine) Solutions. Macromolecules. 2010 Mar 9;43(5):2518–28.

44. Zalusky AS, Olayo-Valles R, Wolf JH, Hillmyer MA. Ordered Nanoporous Polymers from Polystyrene−Polylactide Block Copolymers. J Am Chem Soc. 2002 Oct 1;124(43):12761–73.

45. Li L, Srivastava S, Andreev M, Marciel AB, de Pablo JJ, Tirrell MV. Phase Behavior and Salt Partitioning in Polyelectrolyte Complex Coacervates. Macromolecules. 2018 Apr 24;51(8):2988–95.

46. de la Cruz MO, Belloni L, Delsanti M, Dalbiez JP, Spalla O, Drifford M. Precipitation of highly charged polyelectrolyte solutions in the presence of multivalent salts. J Chem Phys. 1995 Oct 1;103(13):5781–91.

47. Banjade S, Rosen MK. Phase transitions of multivalent proteins can promote clustering of membrane receptors. eLife. 2014 Oct 16;3:e04123.

48. Banjade S, Wu Q, Mittal A, Peeples WB, Pappu RV, Rosen MK. Conserved interdomain linker promotes phase separation of the multivalent adaptor protein Nck. Proc Natl Acad Sci. 2015 Nov 24;112(47):E6426–35.

49. Qin J, de Pablo JJ. Criticality and Connectivity in Macromolecular Charge Complexation. Macromolecules. 2016 Nov 22;49(22):8789–800.

50. Kudlay A, Olvera de la Cruz M. Precipitation of oppositely charged polyelectrolytes in salt solutions. J Chem Phys. 2003 Dec 23;120(1):404–12.

51. Kudlay A, Ermoshkin AV, Olvera de la Cruz M. Complexation of Oppositely Charged Polyelectrolytes: Effect of Ion Pair Formation. Macromolecules. 2004 Nov 1;37(24):9231–41.

52. Castelnovo M, Joanny J-F. Formation of Polyelectrolyte Multilayers. Langmuir. 2000 Sep 1;16(19):7524–32.

53. Lin Y-H, Song J, Forman-Kay JD, Chan HS. Random-phase-approximation theory for sequence-dependent, biologically functional liquid-liquid phase separation of intrinsically disordered proteins. J Mol Liq. 2017 Feb 1;228:176–93.

54. Lin Y-H, Forman-Kay JD, Chan HS. Sequence-Specific Polyampholyte Phase Separation in Membraneless Organelles. Phys Rev Lett. 2016 Oct 17;117(17):178101.

55. Delaney KT, Fredrickson GH. Theory of polyelectrolyte complexation—Complex coacervates are self-coacervates. J Chem Phys. 2017 Jun 14;146(22):224902.

56. Das S, Eisen A, Lin Y-H, Chan HS. A Lattice Model of Charge-Pattern-Dependent Polyampholyte Phase Separation. J Phys Chem B. 2018 May 31;122(21):5418–31.

57. Peterson DW, Zhou H, Dahlquist FW, Lew J. A soluble oligomer of tau associated with fiber formation analyzed by NMR. Biochemistry. 2008 Jul 15;47(28):7393–404.

58. Gustke N, Trinczek B, Biernat J, Mandelkow E-M, Mandelkow E. Domains of tau Protein and Interactions with Microtubules. Biochemistry. 1994 Oct 16;33(32):9511–22.

59. Siow KS, Delmas G, Patterson D. Cloud-point curves in polymer solutions with adjacent upper and lower critical solution temperatures. Macromolecules. 1972;5(1):29–34.

60. Berry J, Weber SC, Vaidya N, Haataja M, Brangwynne CP. RNA transcription modulates phase transition-driven nuclear body assembly. Proc Natl Acad Sci. 2015 Sep 22;112(38):E5237–45.

61. Brangwynne CP, Tompa P, Pappu RV. Polymer physics of intracellular phase transitions. Nat Phys. 2015 Nov;11(11):899–904.

62. Lin Y-H, Forman-Kay JD, Chan HS. Theories for Sequence-Dependent Phase Behaviors of Biomolecular Condensates. Biochemistry. 2018 May 1;57(17):2499–508.

63. Dias CL, Chan HS. Pressure-Dependent Properties of Elementary Hydrophobic Interactions: Ramifications for Activation Properties of Protein Folding. J Phys Chem B. 2014 Jul 10;118(27):7488–509.

64. Dill KA, Alonso DOV, Hutchinson K. Thermal stabilities of globular proteins. Biochemistry. 1989 Jun 27;28(13):5439–49.

65. Doi M, Edwards SF. The Theory of Polymer Dynamics. Clarendon Press; 1988. 420 p.

66. Stockmayer WH. Chain dimensions near the flory temperature. J Polym Sci. 15(80):595–8.

67. Rubinstein M, Colby RH. Polymer Physics. OUP Oxford; 2003. 458 p.

68. Suzuki H, Ohno K, Inagaki H. An estimation of the temperature dependence of the excluded-volume integral. Eur Polym J. 1982 Jan 1;18(3):247–55.

69. Bianconi A, Ciasca G, Tenenbaum A, Battisti A, Campi G. Temperature and solvent dependence of the dynamical landscape of tau protein conformations. J Biol Phys. 2012 Jan 1;38(1):169–79.

70. Danielsen SPO, McCarty J, Shea J-E, Delaney KT, Fredrickson GH. Small Ion Effects on Self-Coacervation Phenomena in Block Polyampholytes. Manuscr Prep. 2018;

71. Gennes P-G de, Gennes PP-G. Scaling Concepts in Polymer Physics. Cornell University Press; 1979. 336 p.

72. Silverstein KAT, Haymet ADJ, Dill KA. The Strength of Hydrogen Bonds in Liquid Water and Around Nonpolar Solutes. J Am Chem Soc. 2000 Aug 23;122(33):8037–41.

73. Makhatadze GI, Privalov PL. Contribution of Hydration to Protein Folding Thermodynamics: I. The Enthalpy of Hydration. J Mol Biol. 1993 Jul 20;232(2):639–59.

74. Matubayasi N. Free-energy analysis of protein solvation with all-atom molecular dynamics simulation combined with a theory of solutions. Curr Opin Struct Biol. 2017 Apr 1;43:45–54.

75. Thirumalai D, Reddy G, Straub JE. Role of Water in Protein Aggregation and Amyloid Polymorphism. Acc Chem Res. 2012 Jan 17;45(1):83–92.

76. Feil H, Bae YH, Feijen J, Kim SW. Effect of comonomer hydrophilicity and ionization on the lower critical solution temperature of N-isopropylacrylamide copolymers. Macromolecules. 1993 May;26(10):2496–500.

77. Choi E, Yethiraj A. Entropic Mechanism for the Lower Critical Solution Temperature of Poly(ethylene oxide) in a Room Temperature Ionic Liquid. ACS Macro Lett. 2015 Jul 21;4(7):799–803.

78. Martin EW, Mittag T. Relationship of Sequence and Phase Separation in Protein Low-Complexity Regions. Biochemistry. 2018 01;57(17):2478–87.

79. Dobrynin AV, Rubinstein M. Counterion Condensation and Phase Separation in Solutions of Hydrophobic Polyelectrolytes. Macromolecules. 2001 Mar 1;34(6):1964–72.

80. Gummel J, Cousin F, Boué F. Counterions Release from Electrostatic Complexes of Polyelectrolytes and Proteins of Opposite Charge: A Direct Measurement. J Am Chem Soc. 2007 May 1;129(18):5806–7.

81. Muthukumar M. Theory of counter-ion condensation on flexible polyelectrolytes: Adsorption mechanism. J Chem Phys. 2004 Apr 29;120(19):9343–50.

82. Hone JHE, Howe AM, Cosgrove T. A Small-Angle Neutron Scattering Study of the Structure of Gelatin/Polyelectrolyte Complexes. Macromolecules. 2000 Feb 1;33(4):1206–12.

83. Lacombe RH, Sanchez IC. Statistical thermodynamics of fluid mixtures. J Phys Chem. 1976 Nov 1;80(23):2568–80.

84. Sanchez IC, Lacombe RH. Statistical Thermodynamics of Polymer Solutions. Macromolecules. 1978 Nov 1;11(6):1145–56.

85. Chang L-W, Lytle TK, Radhakrishna M, Madinya JJ, Vélez J, Sing CE, et al. Sequence and entropy-based control of complex coacervates. Nat Commun. 2017 Nov 2;8(1):1273.

86. Eschmann NA, Georgieva ER, Ganguly P, Borbat PP, Rappaport MD, Akdogan Y, et al. Signature of an aggregation-prone conformation of tau. Sci Rep. 2017 Mar 17;7:44739.

87. Pavlova A, Cheng C-Y, Kinnebrew M, Lew J, Dahlquist FW, Han S. Protein structural and surface water rearrangement constitute major events in the earliest aggregation stages of tau. Proc Natl Acad Sci. 2016;113(2):E127–E136.

88. Finka A, Goloubinoff P. Proteomic data from human cell cultures refine mechanisms of chaperone-mediated protein homeostasis. Cell Stress Chaperones. 2013 Sep;18(5):591–605.

89. Pavlova A, McCarney ER, Peterson DW, Dahlquist FW, Lew J, Han S. Site-specific dynamic nuclear polarization of hydration water as a generally applicable approach to monitor protein aggregation. Phys Chem Chem Phys PCCP. 2009 Aug 21;11(31):6833–9.

90. Elbaum-Garfinkle S, Kim Y, Szczepaniak K, Chen CC-H, Eckmann CR, Myong S, et al. The disordered P granule protein LAF-1 drives phase separation into droplets with tunable viscosity and dynamics. Proc Natl Acad Sci U S A. 2015 Jun 9;112(23):7189–94.

91. Hückel E, Debye P. The theory of electrolytes: I. lowering of freezing point and related phenomena. Phys Z. 1923;24:185–206.

92. Fu J, Schlenoff JB. Driving Forces for Oppositely Charged Polyion Association in Aqueous Solutions: Enthalpic, Entropic, but Not Electrostatic. J Am Chem Soc. 2016 Jan 27;138(3):980–90.

93. Kim S, Huang J, Lee Y, Dutta S, Yoo HY, Jung YM, et al. Complexation and coacervation of like-charged polyelectrolytes inspired by mussels. Proc Natl Acad Sci. 2016 Feb 16;113(7):E847–53.

94. Holehouse AS, Garai K, Lyle N, Vitalis A, Pappu RV. Quantitative Assessments of the Distinct Contributions of Polypeptide Backbone Amides versus Side Chain Groups to Chain Expansion via Chemical Denaturation. J Am Chem Soc. 2015 Mar 4;137(8):2984–95.

95. Kwon H-K, Zwanikken JW, Shull KR, Olvera de la Cruz M. Theoretical Analysis of Multiple Phase Coexistence in Polyelectrolyte Blends. Macromolecules. 2015 Aug 25;48(16):6008–15.

96. Delaney KT, Fredrickson GH. Recent Developments in Fully Fluctuating Field-Theoretic Simulations of Polymer Melts and Solutions. J Phys Chem B. 2016 Aug 11;120(31):7615–34.

97. Advanced Computational Field Theory Methods for Fluctuating Polymer Solutions - ProQuest [Internet]. [cited 2018 Jun 16]. Available from: https://search.proquest.com/openview/4c8b8e54782d4d6d5964834f0bdc88ec/1?pq-origsite=gscholar&cbl=18750&diss=y

98. Fredrickson G. The Equilibrium Theory of Inhomogeneous Polymers. OUP Oxford; 2006. 452 p.

99. Alexander-Katz A, Moreira AG, Sides SW, Fredrickson GH. Field-theoretic simulations of polymer solutions: Finite-size and discretization effects. J Chem Phys. 2004 Dec 13;122(1):014904.

100. Klauder JR. A Langevin approach to fermion and quantum spin correlation functions. J Phys Math Gen. 1983;16(10):L317.

101. Parisi G. On complex probabilities. Phys Lett B. 1983 Nov 17;131(4):393–5.

102. Flory PJ, Volkenstein M. Statistical mechanics of chain molecules. Biopolymers. 8(5):699–700.

103. Villet MC, Fredrickson GH. Efficient field-theoretic simulation of polymer solutions. J Chem Phys. 2014 Dec 12;141(22):224115.

104. Düchs D, Delaney KT, Fredrickson GH. A multi-species exchange model for fully fluctuating polymer field theory simulations. J Chem Phys. 2014 Nov 3;141(17):174103.

Supporting Figure and Table Legends

Figure S1 ThT fluorescence of tau-RNA CC. 100 μM of tau187 and tau187-SL was mixed with 300 μg/mL polyU RNA (RNA) at room temperature. 100 μM tau187 with 25 μM heparin was prepared as reference. Ribbon shows the standard deviation of 3 replicates.

Figure S2 RNase induces turbidity decrease of tau187-RNA CC suspension. Tau187-RNA CCs were re-prepared with 100 μM tau187C291S and 300 μg/mL polyU RNA, while absorbance at 500 nm was monitored. Samples were treated with buffer (Ctrl), 1 U/μL RNase inhibitor (mainly inhibiting RNase A), 50 ng/mL RNase A, and 50 ng/mL RNase A with 1 U/μL RNase inhibitor.

Figure S3 Turbidity of tau-RNA CC at varying charge ratios and ionic strength. (**A**) PolyU RNA was titrated into 20 μM tau187C291S in the buffer of 20 mM ammonium acetate at pH 7. Charge ratio was calculated based on the estimated charge for tau, +11 per tau molecule and the estimated charge for RNA, -1 per nucleotide. Turbidity was assigned from absorbance at λ = 500 nm. Red line indicates the place where the estimated RNA:tau charge ratio equals to 1. (**B**) 20 μM tau was mixed with 60 μg/mL RNA so that RNA:tau charge ratio equals to 1. NaCl was titrated into the mixture while turbidity was monitored.

Figure S4 Turbidity-temperature data and cloud points determinations of various [tau] and [NaCl]. Tau187-RNA CCs were prepared at various concentration of [tau] and [NaCl] with fixed ratio of [RNA]:[tau], shown as strip text (e.g. "2 6 30" refers to [tau] = 2 μM, [RNA] = 6 μg/mL, [NaCl] = 30 mM). Samples were kept at 4 °C before ramping up temperature at 1 °C/min. Absorbance at 500 nm was monitored and used as turbidity (grey points). Turbidity-temperature data were fit to a sigmoid curve (black solid line), where the cloud point, T_{cp}, were determined (blue vertical line). [tau], [NaCl] and T_{cp} were used for theory and simulation modeling.

Figure S5 Phase diagrams of tau114 vs tau187. Tau-RNA CC were prepared with 20 μM tau187 with 60 μg/mL RNA (tau187) or 28 μM tau114 with 84 μg/mL RNA (tau114). **(A)** Turbidity was recorded with varying NaCl concentration. [NaCl] where turbidity vanished were determined by linear fitting to be 131 mM for tau187 and 150 mM for tau114. **(B)** [NaCl] vs. T_{cp} vs. [NaCl] curves for 20 μM tau187 or 28 μM tau114 were computed by FH-VO with $\chi = \chi(T_{cp})$ obtained from Figure 2D, shown together with the experimental data points obtained from (A).

Figure S6 Full phase diagram of tau187-RNA CC. Experimental data showing [tau] vs Tcp was replot from Fig 2B (**points**). Binodal curves was generated by fitting the data to the FH-VO model (**solid lines**).

Figure S7 Determination of phase coexistence points from FTS. (Left). Parametric plot of FTS simulation data points of the osmotic pressure vs the chemical potential. The dilute phase is shown in blue and the concentrated phase (complex coacervate) is shown in red. The intersection point of the two branches is the condition for simultaneous equivalence of pressure and chemical potential for the two phases. (**Right**) The chemical potential vs. the total polymer density from FTS simulation (red points). The horizontal dashed line is the chemical potential at the phase coexistence point. Intersection of the data points with the horizontal dashed lines determines the supernatant (I) and complex-coacervate (II) coexisting polymer densities.

Figure S8 Full phase diagram of tau187-RNA CC from FTS. Low density points (left) are reproduced from Fig. 6 C in the main text. Filled green (low salt) and open green (120 mM NaCl) are obtain from FTS, and red and blue circles are corresponding experimental data. The right side of the figure shows the corresponding high density binodal curve predicted from FTS.

Figure S9 Tau-RNA CC upon addition of heparin. (**A**) 100 μM tau187C291S-SL and 300 μg/mL polyA RNA was mixed in the buffer of 20 mM ammonium acetate at pH 7, with 19 vol % glycerol. Images were taken after 10 minutes at room temperature. (**B**) Sample in A was re-prepared and incubated for 10 min. 25 μM heparin was added afterwards, immediately followed by imaging. The scale bars in both A and B are 50 μm long. **(C)** ThT fluorescences of samples in A and B were monitored with additional 10 μM ThT. **(D)** TEM images of sample in A after overnight incubation, showing no structures similar to amyloid fibrils. **(E)** TEM images of sample in B after overnight incubation, showing structures with length and width consistent with tau fibrils. The scale bars in both D and E are 200 nm long.

Figure S10. Tau *in vitro* phosphorylation. Tau (tau187C291S) were prepared as described in Methods. Tau was subjected to in vitro phosphorylation using mouse brain extract as previously described (Despres, C et. al PNAS 2017). Phosphorylation was confirmed using SDS-PAGE and western blot analysis. Ponceau S staining of the blot shows equal loading of samples before (Tau) and after (P-Tau) the phosphorylation reaction, while reactivity with PHF-1 antibody indicates phosphorylation at S396/404.

Figure S11. Phosphorylation on tau-RNA complex coacervation. A. 20 μM Tau and P-Tau was titrated with PolyU RNA. Absorbance at 500 nm was monitored and plotted as turbidity. **B.** Corresponding representative bright field microscope images of samples in A. **C.** 20 μM Tau and P-Tau was mixed with 50 μg/mL and 100 μg/mL PolyU RNA respectively. Mixtures were titrated with NaCl. Turbidity was plot (solid points) and fit using linear regression (dashed lines). **D.** Corresponding representative bright field microscope images of samples in C.

Table S1 Primary sequences of tau187 and tau114 used in the experiments and VO-FH calculation.

Table S2 Degree of polymerization and average charge densities of species used in the VO-FH calculation. N, degree of polymerization; net charge, estimated net charge per molecule; σ, average charge per monomer.

Table S3 Thermodynamics calculated by VO-FH at 300 K and physiological relevant salt concentrations. T = 300 K was used to determine α, ε_H/T and ε_S. At this temperature, 50 mM ~ 200 mM total salt concentration was used to calculated binodal compositions as described in SI Methods. The calculated composition of tau, RNA and water in the dense phase was listed as ϕ_{tau}+ ϕ_{RNA} and ϕ_{water}. $\Delta H_{D\text{-}H}$, the Debye-Huckel approximated phase separation enthalpy; ΔH, the Flory-Huggins phase separation enthalpy and $T\Delta S$, the Flory-Huggins phase separation entropy.

1286

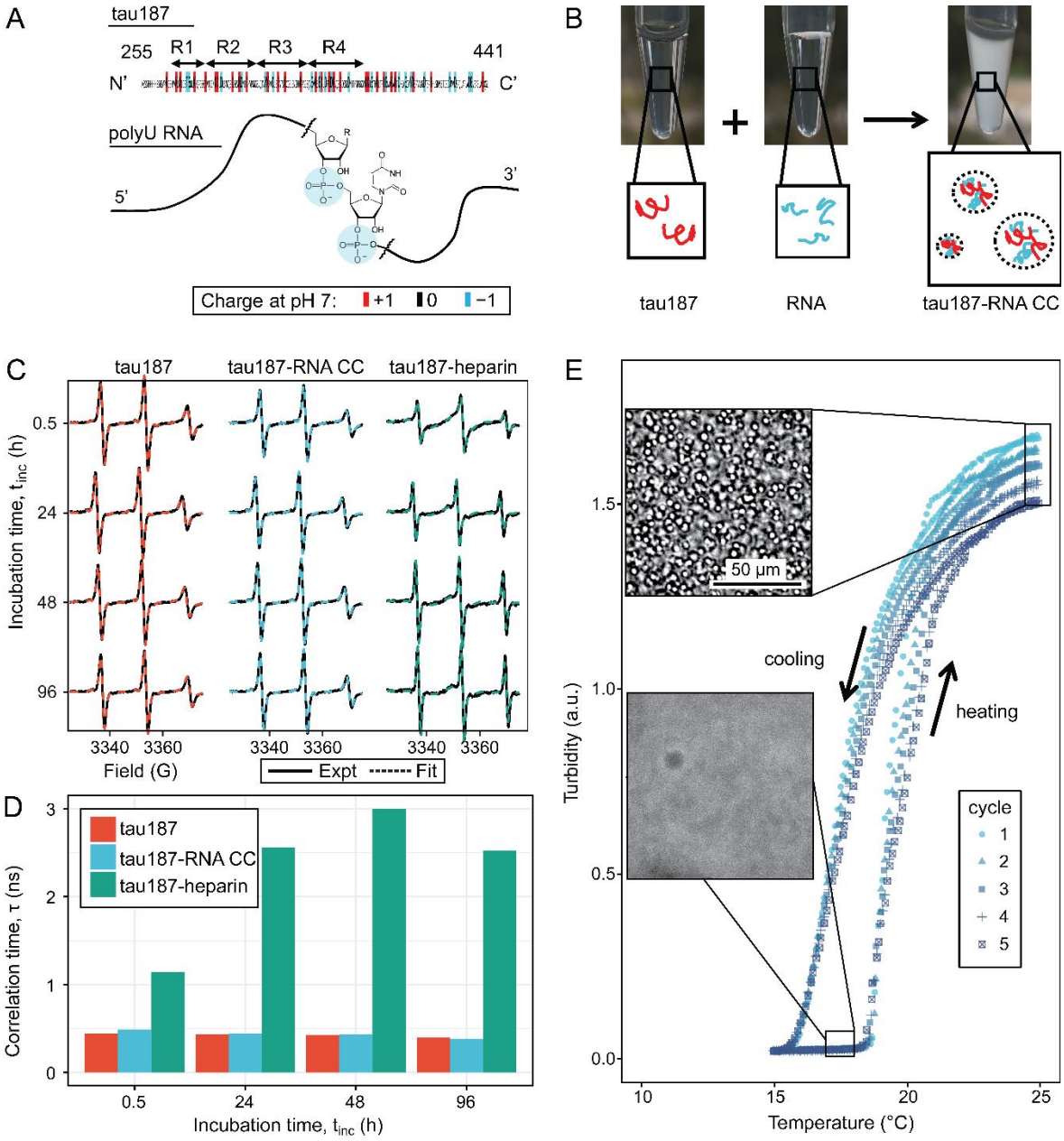

FIG. 1 Steady tau dynamics and reversible droplet formation of tau-RNA complex coacervates. A. Diagram of tau187 (tau) and polyU RNA (RNA). Tau187 is a truncated version of full-length human tau (2N4R 255-441) containing repeat domains and C terminal. At neutral pH experimental conditions, tau187 is overall positively charged; while RNA consists of a phosphate backbone and is negatively charged. **B.** Scheme of tau-RNA CC preparation. Mixing clear tau187 and RNA solutions at proper conditions results in a turbid solution containing liquid

droplets. **C.** X-band cw-EPR spectra (solid line) of tau187 solution (tau187, red), tau187-RNA CC (blue) and tau187-heparin (green) at room temperature with different incubation time, t_{inc}. Samples contains 500 μM tau with 20% spin-labelled. EPR simulation were performed (SI Method) and the fitted spectra is shown as a dashed line. **D.** Rotational correlation time, τ_R extracted from EPR simulation shown in (b1) (SI Method). **E.** Turbidity of tau187-RNA suspension in consecutive heating-cooling cycles. Confocal images represented samples at 19 °C and 25 °C. Temperatures were ramped at 1 °C/min.

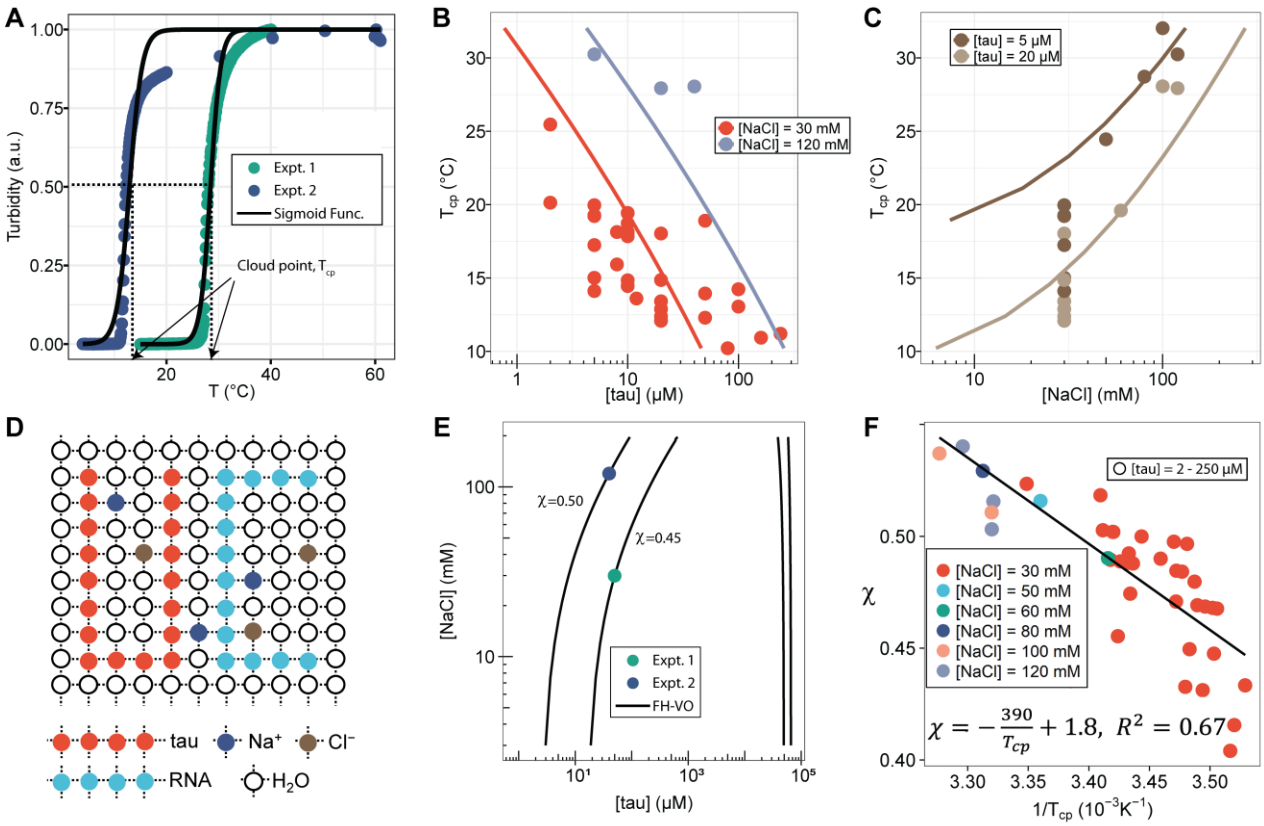

FIG. 2 FH-VO modeling of tau-RNA CC. A. Turbidity of tau187-RNA CC upon heating (Expt.1 ([tau], [NaCl]) = (50 μM, 120 mM), green dots; Expt.2 ([tau], [NaCl]) = (40 μM, 30 mM), purple dots). Absorbance at λ = 500 nm were normalized and used as turbidity value. Turbidity-temperature data of the heating curves were fitted with a sigmoidal function (solid line) as described in (SI Method), and the temperature at which normalized turbidity reaches 0.5 was assigned to cloud point, T_{cp}. **B-C.** Experimental phase diagram (points) showing [tau] vs. T_{cp} and [NaCl] vs. T_{cp} along with the binodal curve generated from fitting the data to the FH-VO model with $\chi = \chi(T_{cp})$ (solid line) **D.** Diagram of Flory Huggins lattice. Tau and RNA are represented by consecutively occupied lattice sites. **E.** Each experimental condition in (**A**) was independently fit to the FH-VO model (solid lines) to obtain an empirical χ value. **E** shows two representative curves**.** These empirically determined values of χ are shown as points in **F.** The

solid line in **F** is a linear regression, generating $\chi = \chi(T_{cp})$, which is then used to generate the binodal lines in **B** and **C**.

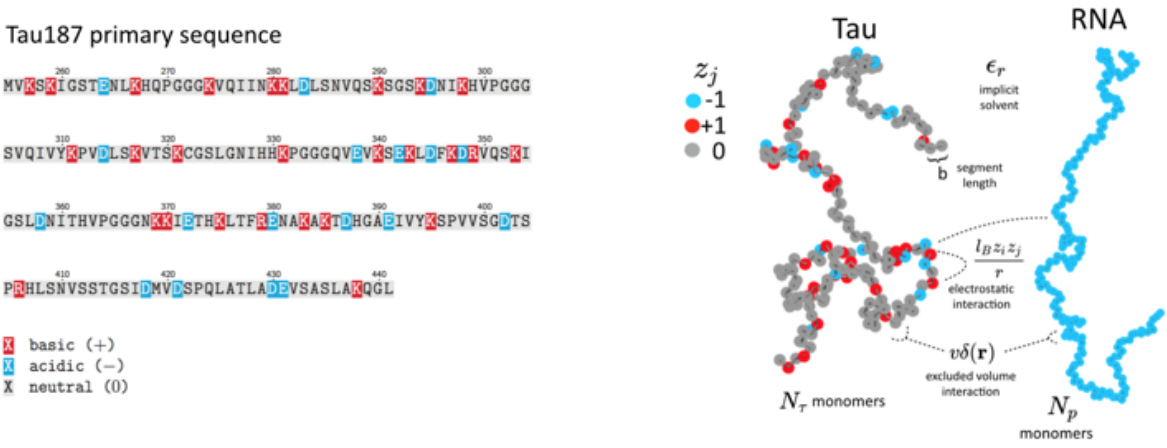

FIG. 3 Schematic depiction of the polyelectrolyte model. Tau and RNA molecules are represented as bead-spring polymers with segment length *b* in implicit solvent. Tau is modeled as a polyampholyte with the charge of each monomer determined from the amino acid charge at pH=7. RNA is modeled as a fully charged polyelectrolyte. In addition to chain connectivity, all monomers interact with an excluded volume repulsive potential, and charged monomers interact with a long-ranged Coulomb potential.

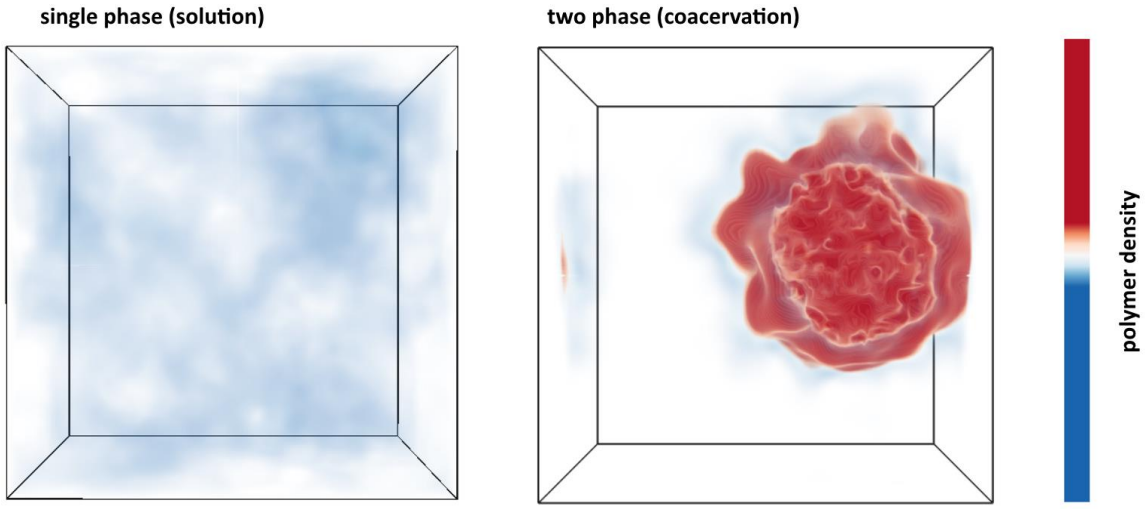

FIG. 4 Polymer density field from FTS. **Left:** Polymer density profile showing a single solution phase for the condition of relatively weak electrostatic strength $l_B = 0.16\ b$ and relatively high excluded volume (good solvent conditions) $v = 0.02\ b^3$. The solution phase is characterized by near homogeneous low polymer density (white/light blue) throughout the entire simulation box. **Right:** Polymer density profile showing complex coacervation upon increasing the electrostatic strength to $l_B = 3.25\ b$ and decreasing the solvent quality by lowering the excluded volume to $v = 0.0068\ b^3$. The two phase region is characterized by a distinct region of high polymer density (dark red) and a surrounding region of low polymer density (white) within the same simulation box. The total polymer concentration is the same in both simulations.

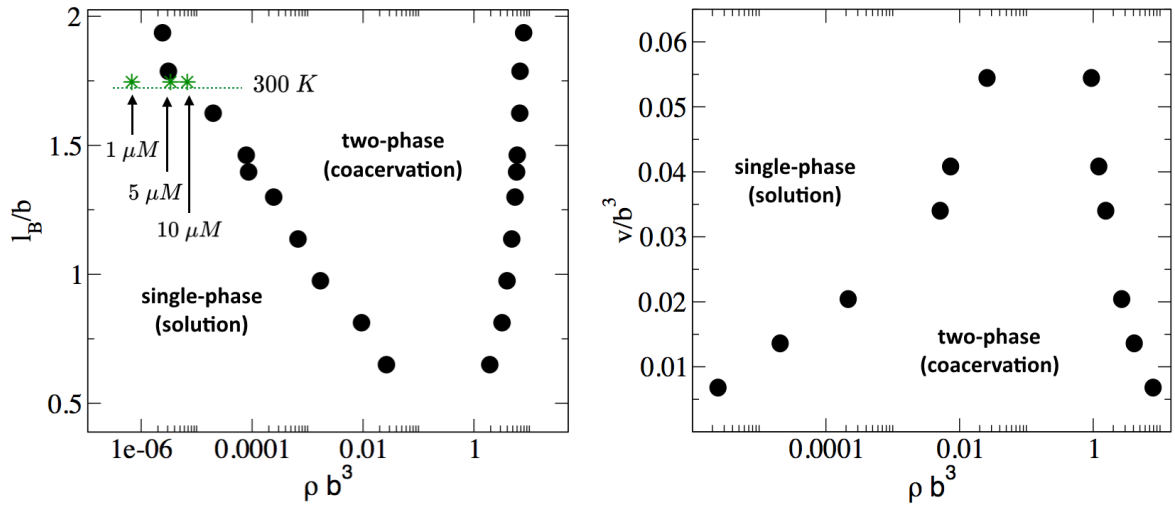

FIG. 5 Phase diagram of the Tau/RNA model obtained from FTS. **(Left)** Binodal points as a function of the Bjerrum length at fixed excluded volume of $v = 0.0068\ b^3$. For comparison three concentrations at 300 K are indicated (arrows) assuming $\epsilon_r = 80$ and $b = 4$ Å **(Right)** Binodal points as a function of the excluded volume at fixed Bjerrum length $l_B = 1.79\ b$

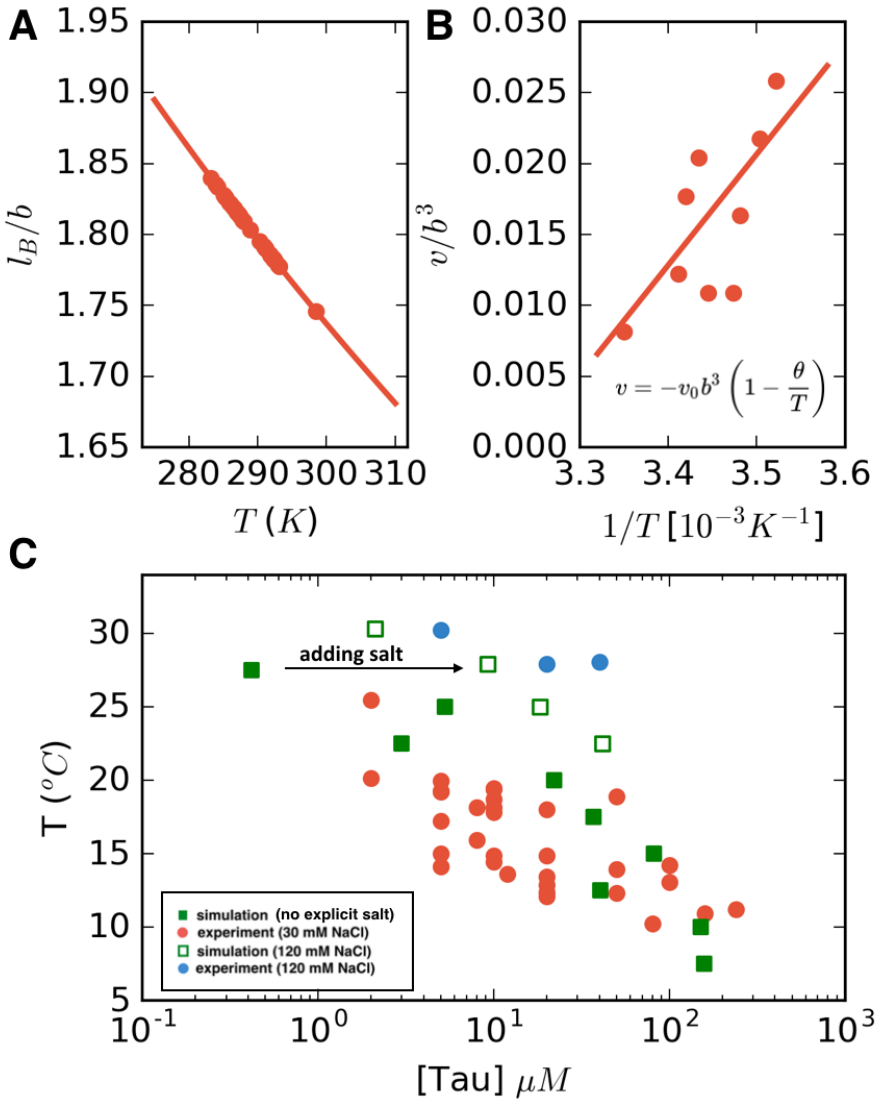

FIG 6 LCST phase behavior from FTS: (**A)** Temperature dependence of the reduced Bjerrum length (ε=80 for water) shown in red. **(B)** Temperature dependence of the excluded volume obtained by adjusting the excluded volume parameter until FTS agrees with a subset of the experimental data (points). The solid line shows a linear fit to the data which is used to obtain the temperature dependent excluded volume for subsequent simulations. **(C)** FTS coexistence points (filled green squares) obtained by using a temperature dependent Bjerrum length (Fig 6A) and excluded volume (Fig 6B). Experiments performed at 20 mM NaCl are shown in red for comparison. Upon introducing excess salt ions in FTS with a fixed

concentration of [NaCl] = 120 mM, the binodal shifts upwards (open green squares). For comparison experiments performed at 120 mM NaCl are shown in blue.

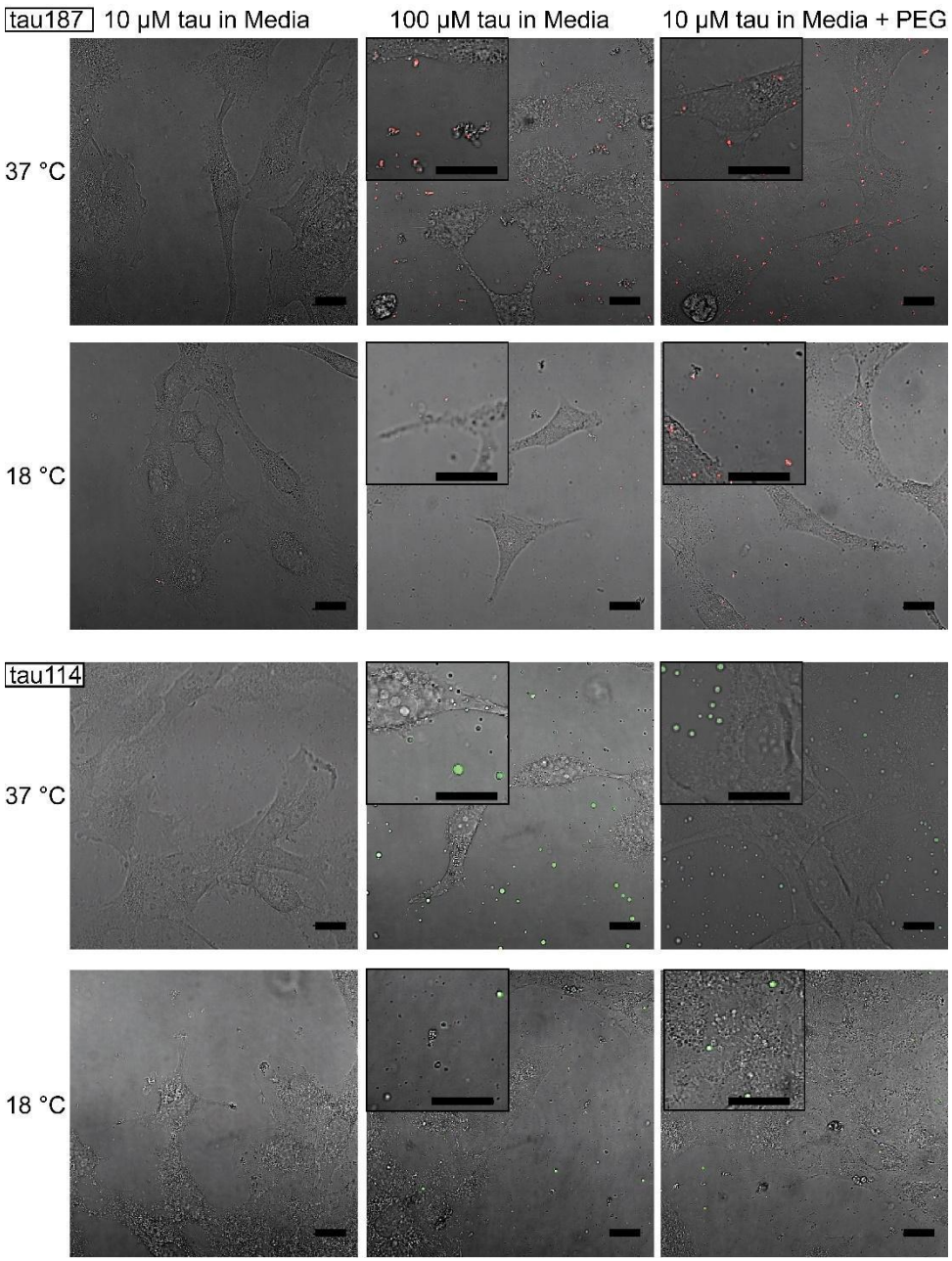

FIG. 7 Tuning experimental conditions to catch tau-RNA complex coacervates in presence of living cells. Bright field images and superimposing fluorescence images of tau-RNA CC coculturing with H4 cells, with 10 μM tau (left), 100 μM tau (middle) and 10 μM tau with 10% v.v. PEG (right). Samples at 37 °C (first row) and 18 °C (second row) were images with representative images showing the co-presence of living cells and tau-RNA CCs. Tau187 (Top)

and tau114 (Bottom) was used showing tau114 with higher propensity at CC formation. Alexa Fluor 488 was used to prepare fluorescent labeled tau. 3 μg/mL polyU RNA per 1 μM tau was used to prepared samples. Scale bar is 20 μm.